bioRxiv preprint doi: https://doi.org/10.1101/2020.02.21.959676; this version posted May 14, 2020. The copyright holder for this preprint (which was not certified by peer review) is the author/funder, who has granted bioRxiv a license to display the preprint in perpetuity. It is made available under aCC-BY-NC-ND 4.0 International license.

Title Page

Title: Inhibitory parvalbumin basket cell activity is selectively reduced during hippocampal sharp wave ripples in a mouse model of familial Alzheimer's disease

Abbrev Title: PVBC activity reduced during SWRs in model of AD

Authors: Adam Caccavano[1*], P. Lorenzo Bozzelli[1], Patrick A. Forcelli[1,2], Daniel T.S. Pak[1,2], Jian-Young Wu[1,3], Katherine Conant[1,3], Stefano Vicini[1,2]

Affiliations: [1]Interdisciplinary Program in Neuroscience, Georgetown University Medical Center, Washington, DC, 20057, [2]Dept. of Pharmacology & Physiology, Georgetown University Medical Center, Washington, DC, 20057, [3]Dept. of Neuroscience, Georgetown University Medical Center, Washington, DC, 20057, *Corresponding Author

Corresponding author email address: ac1625@georgetown.edu

Number of pages: 57

Number of figures, tables: 1 table, 9 figures

Number of words (abstract, significance statement, introduction, discussion): 250; 118; 605; 1492

Conflict of Interest Statement: The authors declare no competing financial interests.

Acknowledgements: AC was supported by NIH/NIA F31 AG062030, NIH/NCATS TL1 TR001431, and the ARCS Foundation. LB was supported by NIH/NINDS T32 NS041218. DP and SV were partially supported by NIH/NIA RF1 AG056603. KC and SV were partially supported by NIH/NINDS R01 NS108810. The content is solely the responsibility of the authors and does not necessarily represent the official views of the National Institutes of Health.

bioRxiv preprint doi: https://doi.org/10.1101/2020.02.21.959676; this version posted May 14, 2020. The copyright holder for this preprint (which was not certified by peer review) is the author/funder, who has granted bioRxiv a license to display the preprint in perpetuity. It is made available under aCC-BY-NC-ND 4.0 International license.

1 **Abstract**

2 Memory disruption in mild cognitive impairment (MCI) and Alzheimer's disease (AD) is poorly
3 understood, particularly at early stages preceding neurodegeneration. In mouse models of AD, there are
4 disruptions to sharp wave ripples (SWRs), hippocampal population events with a critical role in memory
5 consolidation. However, the micro-circuitry underlying these disruptions is under-explored. We tested if
6 a selective reduction in parvalbumin-expressing (PV) inhibitory interneuron activity underlies hyperactivity
7 and SWR disruption. We employed the 5xFAD model of familial AD crossed with mouse lines labeling
8 excitatory pyramidal cells (PCs) and inhibitory PV cells. We observed a 33% increase in frequency, 58%
9 increase in amplitude, and 8% decrease in duration of SWRs in *ex vivo* slices from male and female 3-
10 month 5xFAD mice versus littermate controls. 5xFAD mice of the same age were impaired in a
11 hippocampal-dependent memory task. Concurrent with SWR recordings, we performed calcium imaging,
12 cell-attached, and whole-cell recordings of PC and PV cells within the CA1 region. PCs in 5xFAD mice
13 participated in enlarged ensembles, with superficial PCs having a higher probability of spiking during
14 SWRs. Both deep and superficial PCs displayed an increased synaptic E/I ratio, suggesting a
15 disinhibitory mechanism. In contrast, we observed a 46% spike rate reduction during SWRs in PV basket
16 cells (PVBCs), while PV bistratified and axo-axonic cells were unimpaired. Excitatory synaptic drive to
17 PVBCs was selectively reduced by 50%, resulting in decreased E/I ratio. Considering prior studies of
18 intrinsic PV cell dysfunction in AD, these findings suggest alterations to the PC-PVBC micro-circuit also
19 contribute to impairment.

bioRxiv preprint doi: https://doi.org/10.1101/2020.02.21.959676; this version posted May 14, 2020. The copyright holder for this preprint (which was not certified by peer review) is the author/funder, who has granted bioRxiv a license to display the preprint in perpetuity. It is made available under aCC-BY-NC-ND 4.0 International license.

20 **Significance Statement**

21 We demonstrate that a specific sub-type of inhibitory neuron, parvalbumin-expressing basket cells,
22 have selectively reduced activity in a model of Alzheimer's disease during activity critical for the
23 consolidation of memory. These results identify a potential cellular target for therapeutic intervention to
24 restore aberrant network activity in early amyloid pathology. While parvalbumin cells have previously
25 been identified as a potential therapeutic target, this study for the first time recognizes that other
26 parvalbumin neuronal sub-types, including bistratified and axo-axonic cells, are spared. These
27 experiments are the first to record synaptic and spiking activity during sharp wave ripple events in early
28 amyloid pathology and reveal that a selective decrease in excitatory synaptic drive to parvalbumin basket
29 cells likely underlies reduced function.

bioRxiv preprint doi: https://doi.org/10.1101/2020.02.21.959676; this version posted May 14, 2020. The copyright holder for this preprint (which was not certified by peer review) is the author/funder, who has granted bioRxiv a license to display the preprint in perpetuity. It is made available under aCC-BY-NC-ND 4.0 International license.

30 **Introduction**

31 Alzheimer's disease (AD) is the leading cause of dementia, and a growing public health crisis as
32 worldwide life expectancy increases (Mattson, 2004). AD is characterized by learning and memory
33 deficits, the pathological accumulation of amyloid beta (Aβ) plaques and neurofibrillary tangles, and
34 synaptic and neuronal degeneration (Serrano-Pozo et al., 2011). The cause of memory disruption in the
35 disease is poorly understood, particularly at early ages prior to widespread neurodegeneration. The
36 hippocampus, a region particularly important for the encoding and consolidation of spatial memory, is
37 one of the first regions impaired in AD (Braak and Braak, 1991). Hyperactivity within the hippocampus is
38 observed in mouse models of AD (Palop et al., 2007; Busche et al., 2008, 2012; Palop and Mucke, 2010),
39 as well as in clinical populations, where seizures are an increasingly recognized co-morbidity of AD
40 (Hauser et al., 1986; Amatniek et al., 2006; Palop and Mucke, 2009). While it is well appreciated that Aβ
41 impairs the synaptic function of excitatory pyramidal cells (PCs) in later disease progression (Kamenetz
42 et al., 2003; Shankar et al., 2008; Pozueta et al., 2013), there is growing evidence of early deficits to
43 inhibitory GABAergic cells (Li et al., 2016), potentially explaining this shift to hyperactivity through
44 disinhibition. In particular, several functional impairments are observed in inhibitory parvalbumin-
45 expressing (PV) fast-spiking interneurons (Verret et al., 2012; Mahar et al., 2016; Yang et al., 2016; Hijazi
46 et al., 2019). However, there are at least three distinct PV cell sub-types within the CA1 region of
47 hippocampus with varying anatomical connections and function (Varga et al., 2014), and the separate
48 impact of AD pathology on these sub-types is unknown.

49 PV cells play a critical role in hippocampal sharp wave ripples (SWRs) (Ellender et al., 2010;
50 Schlingloff et al., 2014; Ognjanovski et al., 2017), spontaneous neuronal population events characterized
51 by a low frequency sharp wave (1-30 Hz) and a high frequency ripple (120-250 Hz) (Buzsáki, 1986, 2015;
52 Colgin, 2016). SWRs principally originate in the CA3 region and propagate to CA1 along the Schaffer
53 collaterals, occurring in all mammalian species studied to date (Buzsáki et al., 2013). Even following
54 decortication in brain slices, SWRs spontaneously arise in hippocampus (Buzsáki et al., 1983). SWRs
55 have been extensively studied in large part due to their proposed role in memory consolidation (Wilson
56 and McNaughton, 1994; Kudrimoti et al., 1999; O'Neill et al., 2008; Karlsson and Frank, 2009).

bioRxiv preprint doi: https://doi.org/10.1101/2020.02.21.959676; this version posted May 14, 2020. The copyright holder for this preprint (which was not certified by peer review) is the author/funder, who has granted bioRxiv a license to display the preprint in perpetuity. It is made available under aCC-BY-NC-ND 4.0 International license.

57 Sequences of place cells activated during spatial learning replay in temporally compressed neuronal
58 ensembles within SWRs during rest (Nádasdy et al., 1999; Lee and Wilson, 2002). Online interruption of
59 SWRs through both electrical (Girardeau et al., 2009; Ego-Stengel and Wilson, 2010) and optogenetic
60 stimulation (Ven et al., 2016; Roux et al., 2017) leads to learning and memory deficits, demonstrating
61 their critical role in memory consolidation. Notably, in several mouse models of AD, SWRs are disrupted
62 (Gillespie et al., 2016; Iaccarino et al., 2016; Nicole et al., 2016; Xiao et al., 2017; Hollnagel et al., 2019;
63 Jones et al., 2019; Jura et al., 2019). However, the micro-circuitry underlying these disruptions has yet
64 to be explored in detail. In this study we employed the 5xFAD mouse model of familial Alzheimer's
65 disease crossed with mouse lines that selectively fluoresce in excitatory pyramidal cells (PCs) and
66 inhibitory PV cells. We performed patch clamp recordings of deep and superficial PCs and three distinct
67 PV cell sub-types to record the spiking activity and synaptic input during SWR events in *ex vivo* slices.
68 Our findings support the hypothesis that a preferential reduction in synaptic input and activity of PV basket
69 cells underlies downstream network alterations and suggest that long-term alterations to PC-PVBC
70 micro-circuitry contribute to dysfunction in early amyloid pathology.

bioRxiv preprint doi: https://doi.org/10.1101/2020.02.21.959676; this version posted May 14, 2020. The copyright holder for this preprint (which was not certified by peer review) is the author/funder, who has granted bioRxiv a license to display the preprint in perpetuity. It is made available under aCC-BY-NC-ND 4.0 International license.

71 **Materials and Methods**

72 ***Experimental Animals***

73 To record the activity of excitatory PCs and inhibitory PV cells in amyloid pathology, we employed
74 a combined breeding strategy of transgenic and targeted knockin mice. Transgenic 5xFAD mice
75 (RRID:MMRRC_034840-JAX) (Oakley et al., 2006) were back-crossed for over five generations to the
76 C57BL/6J (RRID:IMSR_JAX:000664) background, which was common to all other strains used. To target
77 the calcium activity of PCs under confocal microscopy, transgenic homozygous Thy1-GCaMP6f-GP5.5
78 (RRID:IMSR_JAX:024276) (Dana et al., 2014) were crossed with hemizygous 5xFAD mice to yield litters
79 with both 5xFAD/+;Thy1-GCaMP6f/+ and Thy1-GCaMP6f/+ littermate controls. PV cells were identified
80 by crossing double homozygous knockin PV^{Cre}/PV^{Cre};tdTom/tdTom (RRID:IMSR_JAX:008069,
81 RRID:IMSR_JAX:007914) (Hippenmeyer et al., 2005; Madisen et al., 2010) with hemizygous 5xFAD mice
82 to yield litters with both 5xFAD/+;PV^{Cre}/+;tdTom/+ and PV^{Cre}/+;tdTom/+ littermate controls. In a subset of
83 experiments the reporter lines were crossed, yielding quadruple transgenic cohorts of 5xFAD/+;Thy1-
84 GCaMP6f/+;PV^{Cre}/+;tdTom/+ and Thy1-GCaMP6f/+;PV^{Cre}/+;tdTom/+ littermate controls. The initial
85 intention was to use a consistent cohort of quadruple transgenic mice for all experiments, yet the breeding
86 strategy proved inhibitive for the number of experiments, thus, patch clamp data were pooled across
87 reporter genotype (Table 1). 5xFAD genotype was assessed at age P7 by tail biopsy via automated
88 genotyping services (Transnetyx, Cordoba, TN, USA). For all experiments, experimenters were blind to
89 5xFAD genotype until after data collection and analysis were fully complete. Mice were weaned at P21
90 and group housed in cages with 3-5 mice separated by sex. As a model of early amyloid pathology prior
91 to neuronal or synaptic loss (Oakley et al., 2006), two experimental cohorts were chosen (each including
92 both males and females) at 1 month (mo) and 3 mo of age. Mice were kept on a standard 12 hr light/dark
93 cycle, food and water were provided *ad libitum*, with all experimental procedures performed in
94 accordance with the guidelines of the Georgetown University Animal Care and Use Committee.

95 ***Amyloid Staining***

96 Mice were anesthetized with isoflurane, transcardially perfused in iced (0º C) PBS and fixed for 48
97 hrs in PFA at 4º C. Brains were then given four 15 min PBS washes, and sliced horizontally at 100 µm

bioRxiv preprint doi: https://doi.org/10.1101/2020.02.21.959676; this version posted May 14, 2020. The copyright holder for this preprint (which was not certified by peer review) is the author/funder, who has granted bioRxiv a license to display the preprint in perpetuity. It is made available under aCC-BY-NC-ND 4.0 International license.

98 thickness with a Vibratome Series 1000. In free floating slices, antigen retrieval was performed for 20 min
99 in a steamer with citrate buffer containing 10 mM $Na_3C_6H_5O_7$, 0.05% Tween20, and pH adjusted to 6.0
100 with HCl. Slices were cooled to room temperature in PBS, then permeabilized for 30 min with 0.5% Triton-
101 X in PBS, given two more PBS rinses, blocked for 2 hrs with 10% NGS and 5% BSA in PBS, and
102 incubated overnight at 4° C with the primary monoclonal mouse antibody MOAB-2 against beta amyloid
103 (1:500; Abcam Cat# ab126649) (Youmans et al., 2012), 0.1% Tween20, 1% NGS, 1% BSA in PBS. The
104 following day slices were given four 15 min PBS washes and incubated in secondary containing Alexa
105 Fluor® 647 conjugated goat anti-mouse IgG (1:500; Jackson Immunoresearch Cat# 115-605-003,
106 RRID:AB_2338902), Thioflavin-S (1:2000; Sigma-Aldrich Cat# T1892), 1% NGS in PBS for 2 hrs at room
107 temperature. Slices were given three more 15 min PBS washes, rinsed in ddH_20, and mounted on slides
108 with Vectashield® antifade mounting medium with DAPI (Vector Laboratories Cat# H-1200,
109 RRID:AB_2336790).

110 ***Behavioral Testing***

111 Hippocampal-dependent learning and memory deficits were assessed by the Barnes maze
112 (Barnes, 1979), with some modifications. The Barnes maze was conducted on a white plastic apparatus
113 (San Diego Instruments) 0.914 m in diameter, with overhead bright illumination (286 lx) serving as the
114 aversive stimulus. The target hole was randomly selected, with four distal visual clues present for
115 visuospatial learning. The training phase consisted of four 180 s trials per day for 4 consecutive days.
116 The probe trial, in which the target hole was inaccessible, was conducted on the fifth consecutive day,
117 consisting of one 90 s trial. Mice were tracked using the ANY-maze tracking system, which was used for
118 distance and speed measurements. The primary measures of latency and number of entries to target
119 hole were hand-scored for increased reliability. Anxiety-like behavior was tested on the elevated plus
120 maze (Pellow et al., 1985). The mice could explore the maze for 5 min, in which time the number of
121 entries and fraction of time in the open arms were assessed by the ANY-maze tracking system. All tests
122 were conducted in the light cycle, at consistent times of the day for each mouse, in an enclosed behavior
123 room with 50 dB ambient sound and 23 lx ambient illumination. Males and females were run on the same

bioRxiv preprint doi: https://doi.org/10.1101/2020.02.21.959676; this version posted May 14, 2020. The copyright holder for this preprint (which was not certified by peer review) is the author/funder, who has granted bioRxiv a license to display the preprint in perpetuity. It is made available under aCC-BY-NC-ND 4.0 International license.

124 day, but in separate groups. Cohorts were not balanced by both sex and genotype, but as much as
125 possible testing order was prepared so that control and 5xFAD mice were alternated.

126 ***Acute Slice Preparation***

127 Brain slices were prepared using NMDG and HEPES-buffered artificial cerebrospinal fluid (aCSF)
128 following a protective recovery protocol (Ting et al., 2014, 2018). Briefly, mice were anesthetized with
129 isoflurane, transcardially perfused, dissected, and sliced in iced (0º C) NMDG-aCSF containing in mM:
130 92 NMDG, 2.5 KCl, 1.25 NaH_2PO_4, 30 $NaHCO_3$, 20 HEPES, 25 Glucose, 10 Sucrose, 5 Ascorbic Acid,
131 2 Thiourea, 3 Sodium Pyruvate, 5 N-acetyl-L-cysteine, 10 $MgSO_4$, 0.5 $CaCl_2$, pH to 7.3-7.4 with HCl (300-
132 310 Osm). All common reagents were obtained from Thermo Fisher Scientific. The brains were sliced
133 horizontally at 500 μm thickness with a Vibratome Series 3000 to preserve hippocampal micro-circuitry
134 and spontaneous SWRs. 3-4 slices were typically obtained per brain, which were bisected so that 6-8
135 hemislices in total were studied per animal. Slices spanned the dorsal-ventral axis, though were primarily
136 medial, as only horizontal slices with intact DG, CA3, and CA1 were retained, ranging from bregma 2-4
137 mm. The slices were transferred together to heated (33º C) NMDG-aCSF, in which Na^+ was gradually
138 introduced along an increasing concentration gradient every 5 min before transferring to room
139 temperature HEPES-aCSF containing in mM: 92 NaCl, 2.5 KCl, 1.25 NaH_2PO_4, 30 $NaHCO_3$, 20 HEPES,
140 25 Glucose, 5 Ascorbic Acid, 2 Thiourea, 3 Sodium Pyruvate, 5 N-acetyl-L-cysteine, 2 $MgSO_4$, 2 $CaCl_2$,
141 pH to 7.3-7.4 with NaOH (300-310 Osm). Slices recovered for 4 hours in a custom-built 150 mL incubation
142 chamber with circulating oxygenated HEPES-aCSF.

143 ***Slice Electrophysiology***

144 Slices were transferred to a Siskiyou PC-H perfusion chamber with a custom-built suspended Lycra
145 thread grid to allow perfusion below and above slice, modeled after (Hájos et al., 2009). Submerged
146 slices were anchored with Warner Instruments slice anchors so that they were sandwiched between two
147 grids, and perfused at a rate of 5 mL/min with heated (30º C) oxygenated aCSF containing in mM: 124
148 NaCl, 3.5 KCl, 1.2 NaH_2PO_4, 26 $NaHCO_3$, 10 Glucose, 1 $MgCl_2$, 2 $CaCl_2$, pH 7.3-7.4 (300-310 Osm).
149 Recordings were conducted with a Multiclamp 700B amplifier (Molecular Devices), digitized at 20 kHz
150 and low-pass Bessel-filtered at 2 kHz with a personal computer running Clampex 11 and a DigiData 1440

bioRxiv preprint doi: https://doi.org/10.1101/2020.02.21.959676; this version posted May 14, 2020. The copyright holder for this preprint (which was not certified by peer review) is the author/funder, who has granted bioRxiv a license to display the preprint in perpetuity. It is made available under aCC-BY-NC-ND 4.0 International license.

151 (Molecular Devices). Two concurrent channels were captured: the local field potential (LFP) was recorded
152 with 0.5-1 MΩ borosilicate pipettes filled with aCSF, paired with 3-5 MΩ borosilicate pipettes for cellular
153 recordings. Cell-attached recordings were performed with aCSF + 5 µM Alexa Fluor® 488 nm (Molecular
154 Probes Cat# A-10440) or 594 nm (Molecular Probes Cat# A-10442) for pipette localization under confocal
155 microscopy. The selected concentration of Alexa dye was below reported alterations to synaptic
156 transmission (Maroteaux and Liu, 2016). Cell-attached recordings were followed with whole-cell
157 recordings of the same cell with a new pipette filled with a Cesium internal, containing in mM: 120
158 $CsMeSO_3$, 5 NaCl, 10 TEA•Cl, 10 HEPES, 1.1 EGTA, 4 QX314, 4 ATP•Na, 0.3 GTP•Na, pH to 7.2 with
159 CsOH (285 Osm). For pipette localization and *post hoc* morphological reconstruction, 5 µM Alexa (either
160 488 or 594 nm) and 0.5% wt/vl biocytin were added to the internal solution on the day of experiment.

161 The LFP electrode was placed in CA1 on the border of *stratum pyramidale* (*str. pyr.*) and *oriens*, a
162 location where both high amplitude sharp waves (SWs) and ripples are simultaneously detectable.
163 Consistent placement of the electrode was attempted in all slices at a depth of ~20 µm. Recordings began
164 10 min after LFP electrode placement to allow slice to recover. If visually detectable SWRs were not
165 observed, the slice was logged as non-SWR producing (Table 1) and discarded. A fluorescent cell was
166 targeted for a loose (20-40 MΩ seal resistance) cell-attached recording of 3-5 min duration. For Thy1-
167 GCaMP6f slices, Ca^{2+} ensemble activity was recorded concurrently with a laser scanning confocal
168 microscope system (Thor Imaging Systems Division) equipped with 488/561/642 nm lasers and
169 green/red/far-red filters and dichroics mounted on an upright Eclipse FN1 microscope (Nikon
170 Instruments). One thousand 512 x 512 pixel frames were captured at a sample rate of 7.5 Hz. A 40x
171 water immersion objective was used, covering an imaging field of 350 x 350 µm, as a balance between
172 maximizing the imaging field while providing sufficient magnification for patch clamp electrophysiology.

173 Following the cell-attached recording, the same cell was targeted with a new Cesium internal
174 electrode. Upon reaching 1 GΩ seal resistance, the membrane was broken by voltage pulse and quick
175 negative pressure. Access resistance was monitored periodically and recordings with a change >20%
176 were discarded. Putative excitatory post-synaptic currents (EPSCs) were measured in voltage-clamp at
177 a holding voltage of -70 mV, and putative inhibitory post-synaptic currents (IPSCs) in the same cell at 0

bioRxiv preprint doi: https://doi.org/10.1101/2020.02.21.959676; this version posted May 14, 2020. The copyright holder for this preprint (which was not certified by peer review) is the author/funder, who has granted bioRxiv a license to display the preprint in perpetuity. It is made available under aCC-BY-NC-ND 4.0 International license.

178 mV. Glutamatergic and GABAergic events were not pharmacologically isolated, as the primary goal was
179 to correlate synaptic activity with spontaneous SWRs, which would be affected by drug administration.
180 The reversal potentials of putative EPSCs and IPSCs matched closely with the expected glutamate and
181 GABA reversal potentials of 0 and -70 mV. This was determined by holding the cell from +20 to -100 mV
182 in 10 mV voltage steps and monitoring the current polarity inversion. Each voltage-clamp recording
183 ranged from 1-3 min. Following PV cell voltage-clamp recordings, the cell was then switched to current-
184 clamp, with current injection to offset the leak current and maintain a membrane potential of -70 mV. 35
185 hyperpolarizing/depolarizing steps of 5 pA increments were delivered to fill the cell with biocytin. A total
186 duration of at least 15 min of whole-cell configuration was maintained, after which an outside-out patch
187 was formed by slowly withdrawing the pipette. Recordings were attempted at -70 and 0 mV for all PCs,
188 while only a subset of PV cells were clamped at 0 mV. The PV cell protocol was initially designed to
189 minimize cell disruption and ensure proper biocytin-filling; however, the recording protocol was revised
190 during the experiment to also record inhibitory input.

191 ***Post Hoc Staining and Microscopy***

192 Slices with biocytin-filled PV cells were returned to the HEPES-aCSF incubation chamber for the
193 remainder of the day, then fixed overnight in 4% PFA, 4% glucose in PBS at 4° C. Slices then received
194 four 15 min PBS washes, 2 hours of permeabilization with 0.5% Triton-X in PBS, 2 PBS rinses, 3 hours
195 in Fluorescein-Avidin (1:500; Vector Laboratories Cat# A-2001, RRID:AB_2336455) in PBS, and four
196 additional 15 min PBS washes. Free floating slices were imaged with a laser scanning confocal
197 microscope system (Thor Imaging Systems Division). Under 20x magnification, z-stacks were obtained
198 covering the span of visible cellular processes (40-80 µm in 1 µm steps), for both green (biocytin) and
199 red (PV^{Cre}-tdTom) channels. In a subset of 14 slices (n_{slice} = 5 Control (CT), 9 5xFAD from n_{mice} = 4 CT,
200 5 5xFAD), an additional round of immuno-staining was performed for Ankyrin G, which labels the axon
201 initial segment of pyramidal cells. A separate subset of Thy1-GCaMP6f slices (n_{slice} = 2 CT, 2 5xFAD
202 each from a separate animal) were stained for Calbindin, with differential expression between superficial
203 and deep PCs. Antigen retrieval was performed on the 500 µm slices for 20 min in a steamer with citrate
204 buffer. Slices were cooled to room temperature for 20 min in PBS, then blocked overnight with 10% NGS

bioRxiv preprint doi: https://doi.org/10.1101/2020.02.21.959676; this version posted May 14, 2020. The copyright holder for this preprint (which was not certified by peer review) is the author/funder, who has granted bioRxiv a license to display the preprint in perpetuity. It is made available under aCC-BY-NC-ND 4.0 International license.

205 at 4° C. The following day the slices were incubated with a primary monoclonal mouse antibody against
206 Ankyrin G (1:100; Thermo Fisher Scientific Cat# 33-8800, RRID:AB_2533145) or Calbindin D-28k
207 (1:1000; Swant Cat# 300, RRID:AB_10000347), 0.1% Tween20, 1% NGS in PBS. After 48 hrs of primary
208 incubation at 4° C, slices were given four 15 min PBS washes and incubated in secondary containing
209 Alexa Fluor® 647 conjugated goat anti-mouse IgG (1:500; Jackson Immunoresearch Cat# 115-605-003,
210 RRID:AB_2338902) and 1% NGS in PBS for 3 hrs at room temperature. Slices were given four more 15
211 min PBS washes, rinsed in ddH_20, and mounted on slides between silicone isolators with Vectashield®
212 mounting medium.

213 ***Pre-processing of Electrophysiology Data and Event Detection***

214 Pre-processing of files was conducted in Clampfit 11 (pClamp, Molecular Devices). Files for
215 calcium imaging experiments were trimmed around the confocal laser trigger signal for alignment of SWR
216 and calcium transients. Spikes were detected in cell-attached recordings with a 3 ms or 1.75 ms template
217 search for PCs or PV cells, respectively. A threshold of 6-8 was used (Clements and Bekkers, 1997) and
218 false negatives minimized (confirmed by manual inspection). False positives were removed by plotting
219 peak vs anti-peak amplitude to segregate noise from true spikes. Bursts were detected with the built-in
220 Burst Analysis, defined as three or more successive spikes, each within 60 or 40 ms (intra-burst interval)
221 for PCs or PV cells, respectively. Spike start, peak, and end times, burst start and end times, number of
222 events in burst, and intra-burst interval were exported from Clampfit for coincidence detection in
223 MATLAB.

224 Whole-cell recordings of post-synaptic current (PSC) signals were low-pass filtered below 1000 Hz
225 with a zero-phase Gaussian FIR filter. PSCs were detected with template searches. Multiple template
226 categories (3-4) of varying duration (ranging from 3-20 ms) were used to improve detection for
227 overlapping PSCs often seen around SWRs. Shorter duration templates used increasingly higher
228 thresholds, between 5-8, to minimize false negatives. Parameters were kept constant for each cell type.
229 PSC results including start, peak, and end times, amplitude, rise tau and decay tau were exported from
230 Clampfit and processed in Microsoft Excel to remove duplicate events with identical peak times. Limits
231 were set on rise and decay tau to remove false positives due to noise. Accepted EPSCs fell within a

bioRxiv preprint doi: https://doi.org/10.1101/2020.02.21.959676; this version posted May 14, 2020. The copyright holder for this preprint (which was not certified by peer review) is the author/funder, who has granted bioRxiv a license to display the preprint in perpetuity. It is made available under aCC-BY-NC-ND 4.0 International license.

232 range of 0.05-5 ms rise tau and 1-50 ms decay tau, while IPSCs fell within a range of 0.1-10 ms rise tau
233 and 3-100 ms decay tau.

234 ***Local Field Analysis and Sharp Wave Ripple Detection***

235 All analysis for coincidence detection between the LFP and cellular events was conducted with
236 custom-built MATLAB functions. Raw traces were imported using the abfload protocol
237 (https://github.com/fcollman/abfload). All applied filters were finite impulse response (FIR) Gaussian filter
238 with constant and corrected phase delays. A wide band-pass (1-1000 Hz) was first applied to remove
239 both low frequency DC drift and high frequency instrument noise. The detection of SWR events was
240 based upon prior approaches (Siapas and Wilson, 1998; Csicsvari et al., 1999; Eschenko et al., 2008),
241 with refinements to minimize false positives and permit additional analyses. The LFP was filtered in both
242 the sharp wave (SW: 1-30 Hz) and ripple (120-220 Hz) ranges, and the root mean square (RMS) was
243 computed every 5 ms in a 10 ms sliding window. The threshold for peak detection was set to 4 standard
244 deviation (SD) above the baseline (lower 0.95 quantile) RMS mean. Event start and end times were set
245 at 2 SD crossings. SWR events were defined as the intersection of concurrent SW and ripple events.
246 The duration of SWR events was determined from the union of concurrent SW and ripple events. The
247 peak of the SWR event was defined as the peak of the SW-RMS signal, and the amplitude as the
248 difference between the peak and baseline values of the SW signal. The power of the SW and ripple were
249 determined by the bandpower MATLAB function of the relevant filtered signal, which computes an
250 approximation of the integral of the power spectral density between the start and end times of the SWR
251 event. Additional filters were applied in the slow gamma (20-50 Hz) and fast/pathological ripple (250-500
252 Hz) ranges, and the power computed on a SWR-event basis, as the power of these SWR-nested
253 oscillations has been implicated in memory performance (Carr et al., 2012) and epileptogenesis (Foffani
254 et al., 2007), respectively.

255 To visualize the spectral components of the LFP as a function of time, spectral analysis was
256 performed for the duration of the recording as well as per SWR event via a Short-Time Fourier Transform
257 (STFT) between 1-500 Hz. To better observe deviations from baseline power, the Z-score for each 1 Hz
258 frequency band was calculated. A Fast-Fourier Transform (FFT) was also computed for a 200 ms window

bioRxiv preprint doi: https://doi.org/10.1101/2020.02.21.959676; this version posted May 14, 2020. The copyright holder for this preprint (which was not certified by peer review) is the author/funder, who has granted bioRxiv a license to display the preprint in perpetuity. It is made available under aCC-BY-NC-ND 4.0 International license.

259 centered around each SWR peak and averaged across all events as an additional visualization of spectral
260 power. The determination of the phase of slow gamma and ripple oscillations during SWRs was based
261 on the analysis of (Varga et al., 2012). Within a 200 ms window centered around the SWR peak, the
262 extrema of the filtered signal of interest were identified, and a piece-wise linear function fit with values
263 from 0º to 180º between a maximum and minimum, 180º to 360º between a minimum and maximum, and
264 then resetting to 0º. The number of cycles within the duration of the SWR event was recorded, from which
265 the peak frequency was calculated as $n_{cycle}/SWR_{duration}$.

266 ***Pre-processing of Ca^{2+} Imaging Data***

267 Raw time series were converted to the change in fluorescence normalized to baseline (*ΔF/F*) with
268 custom-built ImageJ (FIJI) macros, in which batches of raw TIF images were imported with the Bio-
269 Formats plugin (Open Microscopy Environment) and saved as TIF stacks. The TIF stacks were corrected
270 for photo-bleaching via two iterations of the built-in Correct-Bleach plugin. Photo-bleaching was modeled
271 as a sum of two exponentials, a fast 5 s decay and a slower decay over the duration of the recording
272 (133 s). To assist in region-of-interest (ROI) placement, a semi-automated algorithm was applied to
273 highlight regions of highest fluorescence change. For each TIF stack, the squared coefficient of variation
274 (SCV) image was calculated, defined as the variance divided by the average squared for each pixel, or
275 equivalently:

276 $$Img_{SCV} = \frac{1}{n}\sum_{i=1}^{n}\left(\frac{Img_i - \overline{Img}}{\overline{Img}}\right)^2$$

277 Circular ROIs were manually drawn over all identified cells in the SCV image and confirmed with
278 the time series to encompass active cells. Notably, in this way only cells with variable fluorescence were
279 identified, and static highly fluorescent Ca^{2+}-loaded cells were excluded. The *ΔF/F* for each cell was
280 calculated by first subtracting the background fluorescence F_b, defined as the lowest intensity pixel across
281 the entire time series. F_0 for each ROI was defined as the average of the ten images with the lowest
282 intensity. The *ΔF/F* was thus calculated as:

283 $$\Delta F_i / F_0 = \frac{F_i - F_0}{F_0 - F_b}$$

bioRxiv preprint doi: https://doi.org/10.1101/2020.02.21.959676; this version posted May 14, 2020. The copyright holder for this preprint (which was not certified by peer review) is the author/funder, who has granted bioRxiv a license to display the preprint in perpetuity. It is made available under aCC-BY-NC-ND 4.0 International license.

284 These values were exported from ImageJ, along with a separately calculated timing file for each
285 image, computed from a threshold search in Clampfit of the confocal laser trigger channel.

286 ***Calcium Transient Detection and SWR Coincidence Analysis***

287 Automatic detection of calcium transients was performed by first correcting for slow changes in
288 fluorescence, either from remaining photo-bleaching or gradual drift of the imaging plane. A smoothed
289 moving average, calculated with robust locally-weighted regression (Cleveland, 1979) with a window 25%
290 of the file duration (33 s), was subtracted from each *ΔF/F* trace. The baseline-corrected *ΔF/F* traces were
291 interpolated from the raw sampling rate of 7.5 Hz to 2 kHz, and the LFP downsampled from 20 kHz to 2
292 kHz for coincidence detection. Automatic threshold detection for each cell was set at 4 SD above
293 baseline, with the start and end times for each event set at 2 SD. The baseline of each cell was
294 determined by an iterative algorithm of gaussian fitting to the histogram of all data points, which for most
295 cells was a skewed one-tailed distribution with a large baseline peak at zero and a long positive tail
296 representing transient events. For uncommon cells without a skewed distribution (kurtosis < 0), a single
297 gaussian fit was applied to the entire histogram, providing an estimate of the baseline mean and SD.
298 However, for most cells, two iterations were employed, with the first a double-gaussian fit to the entire
299 histogram. The higher amplitude gaussian SD was then used to constrain the upper limit on a second
300 iteration single-gaussian refinement fit of only the baseline. Special logic was necessary in rare situations.
301 For excessively skewed distributions (high *ΔF/F*, kurtosis > 5) the double-gaussian fit was constrained to
302 the lower 0.95 quantile of data. For extremely active cells, because of the slow decay kinetics of GCaMP,
303 the signal peak rivaled or exceeded the baseline peak in amplitude. For these cells, the more negative
304 rather than the higher amplitude peak was used as an estimate of the baseline. In the situation where
305 two peaks were not clearly differentiated (peak separation < 0.1 *ΔF/F*), the gaussian means and SDs
306 were averaged together to arrive at an estimate for constraining the second iteration.

307 Once the baseline mean, SD, and thresholds were determined for each cell, events were detected
308 on a cell-by-cell basis, and characteristics calculated including start, peak, and end times, IEI, duration,
309 amplitude, and frequency. The interpolated calcium traces were trimmed and aligned with the down-
310 sampled LFP trace. Each calcium transient was classified as SWR-coincident if there was any overlap

bioRxiv preprint doi: https://doi.org/10.1101/2020.02.21.959676; this version posted May 14, 2020. The copyright holder for this preprint (which was not certified by peer review) is the author/funder, who has granted bioRxiv a license to display the preprint in perpetuity. It is made available under aCC-BY-NC-ND 4.0 International license.

311 between the start and end of the calcium transient and the start and end of the SWR, otherwise it was
312 classified as spontaneous. Cellular participation during SWRs was assessed by constructing a simplified
313 event matrix with SWRs in one dimension, and cells in the other, with a zero or one if the cell reached
314 threshold during the SWR. For fields with five or more active cells, the ensemble diversity was assessed
315 by calculating the pairwise Jaccard Similarity index between SWR events, ranging from a value of zero
316 if two SWR events had no cells in common, to a value of one if all cellular participants were identical,
317 modeled after the analysis of (Miyawaki et al., 2014). The cell-cell pairwise index was also calculated,
318 ranging from zero if two cells never participated in the same SWR events, to one if they participated in
319 precisely the same SWRs. The cumulative distribution functions were determined for each recording by
320 considering all off-diagonal values in one half of the symmetric similarity matrices.

321 ***Spike and SWR Coincidence Analysis***

322 Each spike/burst was classified as SWR-coincident if there was any overlap between the start and
323 end of the spike/burst and the start and end of the SWR, otherwise it was classified as spontaneous. To
324 examine spike rate in more detail around SWR events, the peri-SWR spike probability was calculated by
325 sorting all spikes that occurred within a 200 ms window centered around each SWR peak into 2 ms bins
326 and normalizing to all SWR events. Spike-phase coupling was determined by identifying the previously
327 calculated gamma and ripple phases at the spike peak time. Spike phase times were only considered for
328 further analysis if trough-peak amplitude exceeded 4 SD of the gamma or ripple signal.

329 ***Post-Synaptic Current and SWR Coincidence Analysis***

330 Each EPSC/IPSC was classified as SWR-coincident (swrEPSC/swrIPSC) if there was any overlap
331 between the start and end of the event and a 100 ms window centered around each SWR peak, otherwise
332 it was classified as spontaneous (sEPSC/sIPSCs). The more conservative window to classify
333 spontaneous events (compared to the calcium and spike analysis) better captured the buildup of
334 EPSCs/IPSCs preceding SWRs (Schlingloff et al., 2014). As events overlap and complicate detection
335 during SWRs, for quantification the current was integrated in a 100 ms window centered at the SWR
336 peak to determine the total charge (swrEPSQ/swrIPSQ). To examine the distribution of sEPSCs/sIPSCs,
337 the cumulative distribution function of all events was computed for each cell and averaged across all cells

bioRxiv preprint doi: https://doi.org/10.1101/2020.02.21.959676; this version posted May 14, 2020. The copyright holder for this preprint (which was not certified by peer review) is the author/funder, who has granted bioRxiv a license to display the preprint in perpetuity. It is made available under aCC-BY-NC-ND 4.0 International license.

338 in a group. For a view of the temporal progression of synaptic input during SWRs, the charge was also
339 calculated by integrating a sliding 100 ms window every 2 ms in a 200 ms window centered around the
340 SWR peak.

341 ***Experimental Design and Statistical Analyses***

342 Most experiments in this study have been presented in a case-control experimental design, in which
343 data from 5xFAD mice are compared to littermate controls. With behavioral learning on the Barnes Maze
344 we have employed a longitudinal repeated measures (RM) design. In analyzing the impact of factors on
345 LFP activity in a large sample of *ex vivo* slices, we have taken a factorial design. All data were tested for
346 normality and lognormality via Shapiro-Wilk tests. If all groups were normally distributed, they were
347 analyzed with parametric tests (unpaired t-test, n-way ANOVA, n-way RM ANOVA) and have been
348 displayed on bar plots with error bars representing the mean ± SEM. If any group was not normally
349 distributed, the data have been presented on box-whisker or violin plots, with lines indicating median and
350 quartiles, and full error bars representing range. If all groups were lognormally distributed, the data were
351 log transformed, the results of which were analyzed with parametric tests, with the log-means compared.
352 For clarity, the original non-transformed data have been displayed in plots. If any group was neither
353 normal nor lognormal, non-parametric statistical tests of rank were employed. Circular data (phase
354 angles) were analyzed with a similar approach. Data were tested for non-uniformity via a Rayleigh test
355 to determine if they could be sampled from a von Mises (circular normal) distribution. If the Rayleigh test
356 reached significance for all groups, means were compared with the Watson-Williams test, otherwise a
357 circular median test was performed.

358 The particular statistical tests used are listed in the Results. Any values cited in the text are mean
359 ± SEM. All *post hoc* multiple comparisons used the Šidák correction (ŠC). Within each plot all individual
360 data points are presented. No data were excluded based on their values, but only for experimental
361 reasons (e.g. no SWRs present, excessive slice movement, unstable patch clamp recording). The n is
362 indicated in the text and figure legends, and differs between experiment, either n_{mice}, n_{slice}, or n_{cell}. Raw p-
363 values are displayed in plots; if less than a significance level of 0.05 they are bold. Data originating from
364 male or female mice are presented as closed or open circles, respectively. Sex differences were

bioRxiv preprint doi: https://doi.org/10.1101/2020.02.21.959676; this version posted May 14, 2020. The copyright holder for this preprint (which was not certified by peer review) is the author/funder, who has granted bioRxiv a license to display the preprint in perpetuity. It is made available under aCC-BY-NC-ND 4.0 International license.

365 examined for some endpoints, but in general the experiments were insufficiently powered to determine
366 sex differences. A power analysis of the principal experiments was performed based on preliminary data,
367 guiding the number of animals/cells chosen.

368 Graphpad Prism 8 was used for all 1 and 2-sample statistical tests. Microsoft Excel and MATLAB
369 2019 were used for some simple calculations of mean, SD, SEM, ratio, and error propagation. n-way
370 ANOVAs were performed in the Statistics and Machine Learning Toolbox of MATLAB 2019. Non-
371 parametric factorial data were aligned and ranked with ARTool (Wobbrock et al., 2011), before running
372 ANOVAs. Circular statistics were run in the Circular Statistics Toolbox for MATLAB (Berens, 2009).

373 ***Code Accessibility***

374 All code is open-source and available in public repositories, including versions under active
375 development (Github) as well as archival copies used for this manuscript (Zenodo). MATLAB functions
376 are available at https://github.com/acaccavano/SWR-Analysis (archival copy: DOI: 10.5281/zenodo.
377 3625236). ImageJ (FIJI) macros are available at https://github.com/acaccavano/deltaFoF (archival copy:
378 DOI: 10.5281/zenodo.3625130).

bioRxiv preprint doi: https://doi.org/10.1101/2020.02.21.959676; this version posted May 14, 2020. The copyright holder for this preprint (which was not certified by peer review) is the author/funder, who has granted bioRxiv a license to display the preprint in perpetuity. It is made available under aCC-BY-NC-ND 4.0 International license.

379 **Results**

380 ***Three month 5xFAD mice deposit amyloid and display minor impairment in spatial memory***

381 The 5xFAD model of familial Alzheimer's disease is an aggressive though useful model of amyloid
382 pathology, as it exhibits heavy amyloid accumulation in hippocampus and associated cortices, and is
383 accompanied with memory impairment (Oakley et al., 2006). 5xFAD mice are unimpaired in performance
384 on the T-maze at 2 months (mo) but become impaired by 4-5 mo when amyloid burden is greater (Oakley
385 et al., 2006). Interestingly, at 3 mo there is no evidence for neuronal or synaptic degeneration, while
386 several synaptic markers begin to decline at 4 mo and are significantly reduced from controls by 9 mo.
387 We observed intracellular amyloid accumulation in the subiculum and CA1 region of hippocampus in 1
388 mo 5xFAD mice without the presence of extracellular plaques (n_{mice} = 2 Control (CT), 2 5xFAD), while in
389 3 mo 5xFAD mice we observed multiple extracellular plaques in subiculum, with sparse plaques in CA1
390 (n_{mice} = 2 CT, 2 5xFAD, Fig. 1A). Prior work indicates that amyloid burden continues to increase
391 throughout the lifespan of 5xFAD mice (Oakley et al., 2006; Youmans et al., 2012).

392 In separate 1 mo (n_{mice} = 10 CT, 10 5xFAD) and 3 mo cohorts (n_{mice} = 15 CT, 12 5xFAD, Table 1),
393 we examined the performance of 5xFAD mice and littermate controls on the Barnes Maze. Both age
394 cohorts learned the task, as seen by decreased latency to find escape hole over progressive days of
395 training, and a significant effect of training day (1 mo: $F_{(3,54)} = 23.9$, $p = 5.7 \times 10^{-10}$; 3 mo: $F_{(3,75)} = 31.6$, p
396 = 2.7×10^{-13}; 2-way Repeated Measures (RM) ANOVA, align-rank transformed (ART); Fig. 1B). There
397 were no differences observed in training between genotype for either the 1 mo cohort ($F_{(1,18)} = 0.096$, p
398 = 0.760) or the 3 mo cohort ($F_{(1,25)} = 1.086$, p = 0.307), nor were there interactions of genotype × training
399 day (1 mo: $F_{(3,54)} = 0.496$, p = 0.687; 3 mo: $F_{(3,75)} = 0.983$, p = 0.405). On the probe day, 1 mo 5xFAD
400 mice had similar latencies to controls (U = 46, p = 0.781; Mann-Whitney; Fig. 1C), while 3 mo 5xFAD
401 mice had a longer latency to find the escape hole from 18.4 ± 7.6 s to 37.4 ± 9.8 s (U = 48, p = 0.040;
402 Mann-Whitney; Fig. 1C-D). The number of entries to the area of the escape hole, another commonly
403 reported endpoint, was not significantly different for either cohort (1 mo: $t_{(18)} = 0.735$, p = 0.472; 3 mo: $t_{(25)}$
404 = 0.691, p = 0.496; unpaired t-tests). 5xFAD mice displayed no obvious motor impairments, as the total
405 distance traveled did not differ between genotype at either age (1 mo: 3.98 ± 0.91 m (CT), 3.77 ± 0.49 m

bioRxiv preprint doi: https://doi.org/10.1101/2020.02.21.959676; this version posted May 14, 2020. The copyright holder for this preprint (which was not certified by peer review) is the author/funder, who has granted bioRxiv a license to display the preprint in perpetuity. It is made available under aCC-BY-NC-ND 4.0 International license.

406 (5xFAD), $t_{(18)}$ = 0.203, p = 0.842; 3 mo: 3.98 ± 0.49 m (CT), 3.40 ± 0.49 m (5xFAD), $t_{(25)}$ = 0.816, p =
407 0.422; unpaired t-tests), neither did the mean speed (1 mo: 4.4 ± 1.0 cm/s (CT), 4.2 ± 0.5 cm/s (5xFAD),
408 $t_{(18)}$ = 0.186, p = 0.856; 3 mo: 4.4 ± 0.6 cm/s (CT), 3.8 ± 0.5 cm/s (5xFAD), $t_{(25)}$ = 0.819, p = 0.420;
409 unpaired t-tests).

410 To test if this observed memory impairment could be attributed to altered anxiety-like behavior, the
411 cohorts were also tested on the Elevated Plus Maze. Neither age cohort showed a significant difference
412 in fraction of time spent in open arms (1 mo: 15.4 ± 2.2% (CT), 15.1 ± 0.9% (5xFAD), $t_{(18)}$ = 0.129, p =
413 0.900; 3 mo: 10.7 ± 1.0 (CT), 9.3 ± 1.5 (5xFAD), $t_{(25)}$ = 0.848, p = 0.404; unpaired t-tests), nor in number
414 of open arm entries (1 mo: 7.9 ± 0.6 (CT), 7.4 ± 0.6 (5xFAD), $t_{(18)}$ = 0.570, p = 0.576; 3 mo: 9.2 ± 0.7
415 (CT), 7.5 ± 0.6 (5xFAD), $t_{(25)}$ = 1.863, p = 0.074; unpaired t-tests). Therefore, we concluded that 3 mo
416 5xFAD mice on our genetic background had a mild spatial memory impairment. As memory impairment
417 has been widely reported in 5xFAD mice at later ages (Oakley et al., 2006; Ohno, 2009; Tohda et al.,
418 2012), no further memory tasks were performed.

419 ***Sharp wave ripples are increased in 3 month 5xFAD mice***

420 As spatial memory relies heavily on the activity of the hippocampus, and sharp wave ripples
421 (SWRs) are critical for the consolidation of new memories (Buzsáki, 1986; Wilson and McNaughton,
422 1994), we next recorded spontaneous SWRs in hippocampal slices from control and 5xFAD mice (Fig.
423 2A-B). SWRs were recorded in the CA1 region in multiple slices for each animal and averaged in both a
424 1 mo cohort (n_{mice} = 10 CT, 10 5xFAD), and a 3 mo cohort (n_{mice} = 27 CT, 29 5xFAD, Table 1). While the
425 electrode placement was kept as consistent as possible across recordings (see Methods), slight
426 deviations in placement can result in large variance in the LFP. We attempted to control for this by
427 recording from many slices (1 mo: n_{slice} = 51 CT, 45 5xFAD; 3 mo: n_{slice} = 101 CT, 88 5xFAD) and then
428 averaging across slices for each animal. In the 1 mo cohort, the SWR event frequency did not differ ($t_{(18)}$
429 = 0.946, p = 0.357; unpaired t-test; Fig. 2C), nor were there changes for any other LFP endpoints (data
430 not shown). However, in the 3 mo cohort, SWR event frequency was increased in 5xFAD mice versus
431 controls from 0.94 ± 0.07 Hz to 1.25 ± 0.08 Hz ($t_{(54)}$ = 2.89, p = 0.006; unpaired t-test; Fig. 2C). We next
432 verified if there was an altered percentage of slices exhibiting SWRs in 5xFAD mice (Table 1), as this

bioRxiv preprint doi: https://doi.org/10.1101/2020.02.21.959676; this version posted May 14, 2020. The copyright holder for this preprint (which was not certified by peer review) is the author/funder, who has granted bioRxiv a license to display the preprint in perpetuity. It is made available under aCC-BY-NC-ND 4.0 International license.

433 could underlie observed differences in event frequency. While a 2-way ANOVA revealed a significant
434 effect of 5xFAD genotype ($F_{(1,72)}$ = 6.51, p = 0.013) and age ($F_{(1,72)}$ = 5.21, p = 0.0254) on percentage of
435 slices with SWRs, the only significant difference observed when corrected for multiple comparisons was
436 between control slices at 1 mo and 3 mo (p = 0.039, Šidák correction (ŠC)), while 3 mo slices did not
437 differ between genotype (p = 0.759, ŠC). Therefore, the observed differences in 3 mo mice are not likely
438 due to altered viability of the slices.

439 In addition to an increased event frequency, SWR amplitude was increased by 58 ± 17% in 3 mo
440 5xFAD mice ($t_{(48.9)}$ = 3.59, p = 0.0008; Welch's t-test) and surprisingly were 3.7 ± 1.2 ms shorter in duration
441 ($t_{(54)}$ = 3.18, p = 0.0025; unpaired t-test; Fig. 2D). This decrease in duration was likely attributable to both
442 increased peak ripple frequency ($t_{(54)}$ = 3.422 p = 0.0012; unpaired t-test) and decreased number of
443 complete ripple cycles ($t_{(54)}$ = 3.48, p = 0.016; unpaired t-test; Fig. 2E), and is of interest as longer duration
444 SWRs have been demonstrated to improve memory (Fernández-Ruiz et al., 2019). Spectral features of
445 SWRs also differed between genotype (Fig. 2F-J). Low-gamma (20-50 Hz) nested within SWRs,
446 speculated to play a role in coordinating CA3 and CA1 memory replay (Carr et al., 2012), was increased
447 in 5xFAD mice (U = 193, p = 0.0009, Mann-Whitney; Fig. 2H). While the ripple peak frequency was shifted
448 (Fig. 2E,G), the total power within the ripple frequency range from 120-220 Hz was unchanged (U = 358,
449 p = 0.591; Mann-Whitney; Fig. 2I). The power of fast or pathological ripples (250-500 Hz) did not differ
450 between 5xFAD and control slices (U = 379, p = 0.845; Mann-Whitney; Fig. 2J), suggesting the increased
451 activity in 5xFAD slices was distinct from epileptiform activity (Foffani et al., 2007).

452 Spontaneous SWRs recordings were repeated in three separate 3 mo sub-cohorts with different
453 reporter mouse lines for subsequent patch-clamp and Ca^{2+} imaging experiments (Table 1). SWR
454 frequency increased in 5xFAD mice in both larger cohorts: PV^{Cre}/+;tdTom/+ mice (135 ± 18%, n_{mice} = 13
455 CT, 11 5xFAD) and Thy1-GCaMP6f mice (156 ± 21%, n_{mice} = 10 CT, 11 5xFAD). In the third smaller
456 Thy1-GCaMP6f;PV^{Cre}/+;tdTom/+ cohort, there was no significant increase observed (93 ± 18%, n_{mice} = 4
457 CT, 7 5xFAD). A 2-way ANOVA for 5xFAD genotype and reporter line revealed only a significant effect
458 of 5xFAD genotype ($F_{(1,50)}$ = 5.41, p = 0.024) and not reporter line ($F_{(2,50)}$ = 1.50, p = 0.233) nor interaction
459 term ($F_{(2,50)}$ = 2.06, p = 0.138). The data for the three sub-cohorts were therefore pooled into the results

bioRxiv preprint doi: https://doi.org/10.1101/2020.02.21.959676; this version posted May 14, 2020. The copyright holder for this preprint (which was not certified by peer review) is the author/funder, who has granted bioRxiv a license to display the preprint in perpetuity. It is made available under aCC-BY-NC-ND 4.0 International license.

460 presented in (Fig. 2), and in subsequent patch clamp experiments, with the lack of phenotype in the
461 quadruple transgenic cohort likely attributable to smaller sampling. To test if sex, brain hemisphere, and
462 dorsal-ventral slice position had an effect, an additional 4-way ANOVA of all slices was performed. A
463 small effect of 5xFAD genotype was found (n_{slice} = 101 CT, 88 5xFAD; $F_{(1,178)} = 10.4$, $p = 0.0015$), and a
464 small effect of dorsal-ventral position ($F_{(1,178)} = 10.46$, $p = 0.0015$), with ventral slices (bregma 3-4 mm)
465 126 ± 12% the frequency of more dorsal slices (bregma 2-3 mm) for both control and 5xFAD slices.
466 Correcting for multiple comparisons, within each genotype the difference between dorsal and ventral
467 slices did not reach significance (D vs V: $p = 0.078$ (CT), $p = 0.235$ (5xFAD), ŠC). No significant effects
468 were observed for sex ($F_{(1,178)} = 0.728$, $p = 0.395$), brain hemisphere ($F_{(1,178)} = 0.873$, $p = 0.351$), nor any
469 interaction terms.

470 ***Altered ensembles of pyramidal cells are recruited in 5xFAD slices***

471 The replay of pyramidal cell (PC) ensembles during SWRs is critical for the consolidation of spatial
472 memory (Wilson and McNaughton, 1994; Skaggs and McNaughton, 1996; Lee and Wilson, 2002; O'Neill
473 et al., 2008). Given the observed alterations to SWRs in 3 mo 5xFAD mice, we next sought to determine
474 if ensembles of PCs were altered via calcium imaging (Fig. 3A). PCs differentiate into superficial (sPCs,
475 closer to *str. radiatum*) and deep (dPCs, closer to *str. oriens*) cells, with different function, connectivity,
476 and molecular profiles (Lee et al., 2014; Valero et al., 2015). We distinguished sPCs and dPCs via *post*
477 *hoc* staining of imaged slices for calbindin (CB), which is more highly expressed in sPCs. While dorsal
478 hippocampus exhibits a clear delineation of CB+ sPCs and CB- dPCs (Lee et al., 2014), we observed a
479 CB bilayer in our slices (Fig. 3B), as previously reported in more ventral hippocampus (Baimbridge and
480 Miller, 1982; Slomianka et al., 2011). In $n_{slice} = 4$ from n_{mice} = 2 CT, 2 5xFAD, we counted the total number
481 of GCaMP (GC)+ CB- (539), GC- CB+ (292) and GC+ CB+ (146) cells, and for each calculated the
482 distance from the border of *str. radiatum* and *pyramidale* (Fig. 3C). At 30 μm there was a switch from
483 majority CB+ to GC+ cells, with a non-trivial fraction of double-labeled GC+ CB+ cells: 17.9% from 0 - 30
484 μm and 15.7% from 30 - 90 μm. At depths greater than 90 μm there was lower co-expression of 7.9%.
485 All subsequent experiments were performed on GC+ cells with a cutoff of 30 μm between putative sPCs
486 and dPCs.

bioRxiv preprint doi: https://doi.org/10.1101/2020.02.21.959676; this version posted May 14, 2020. The copyright holder for this preprint (which was not certified by peer review) is the author/funder, who has granted bioRxiv a license to display the preprint in perpetuity. It is made available under aCC-BY-NC-ND 4.0 International license.

487 The ensemble activity of PCs was recorded under confocal microscopy in slices from 488 5xFAD/+;Thy1-GCaMP6f mice and Thy1-GCaMP6f littermate controls (Fig. 3D). Active cells were 489 detected with a semi-automated algorithm and both spontaneous and SWR-coincident Ca^{2+} transient 490 events were detected. Within 5xFAD slices, the total number of active PCs detected per imaging field 491 was increased from 17.0 ± 2.6 to 24.0 ± 1.6 PCs in n_{slice} = 25 CT, 23 5xFAD ($t_{(31.2)}$ = 3.091, p = 0.0042; 492 Welch's t-test, log-transformed (LT)), with a greater number of PCs active during SWRs (CT: 3.6 ± 0.6, 493 5xFAD: 4.9 ± 0.8 cells, $t_{(40.1)}$ = 2.063, p = 0.046; Welch's t-test, LT). When delineated by PC sub-type, 494 there was a significant effect of genotype on the number of active cells ($F_{(1,92)}$ = 11.8, p = 0.00088; 2-way 495 ANOVA, ART; Fig. 3E), as well as an effect of cell type ($F_{(1,92)}$ = 20.6, p = 1.7 × 10^{-5}). The number of sPCs 496 was increased in 5xFAD slices from 5.7 ± 0.8 to 8.7 ± 1.0 cells (p = 0.067, ŠC) and dPCs from 11.3 ± 2.0 497 to 15.6 ± 1.2 cells (p = 0.039, ŠC), with significantly more dPCs than sPCs for both genotypes (CT: p = 498 0.014; 5xFAD: p = 0.00041, ŠC). During SWRs, more dPCs participated than sPCs ($F_{(1,87)}$ = 12.19, p = 499 0.00076; 2-way ANOVA, ART; Fig. 3F) in both CT (p = 0.0063, ŠC) and 5xFAD slices (p = 0.00095, ŠC). 500 However, no effect of genotype was observed ($F_{(1,87)}$ = 0.747, p = 0.390), in contrast to the increase 501 observed when considering all PCs together.

502 We next asked if characteristics of the Ca^{2+} events differed between genotype, as an indirect 503 measure PC firing activity. Averaging across cells from each slice, no differences were found in the 504 frequency ($F_{(1,87)}$ = 0.094, p = 0.759; 2-way ANOVA, log-transformed (LT); Fig. 3G), amplitude ($F_{(1,87)}$ = 505 0.093, p = 0.761; 2-way ANOVA, LT; Fig. 3H), nor duration of Ca^{2+} transient events ($F_{(1,87)}$ = 0.289, p = 506 0.593; 2-way ANOVA, LT; Fig. 3I). This suggests that on an individual cell level, PCs exhibit similar 507 activity in 5xFAD mice as compared to controls, with differences only becoming apparent on the 508 ensemble level. Finally, we sought to determine if the cellular composition of PC ensembles during SWR 509 events was altered. Ensemble diversity was assessed by calculating the pairwise Jaccard similarity of 510 cellular participation between all SWR events (Fig. 3J). Additionally, the Jaccard similarity of SWR 511 participation between cells was computed between sPCs/dPCs and all other PCs (Fig. 3J, bottom right). 512 The cumulative distribution functions of all pairwise comparisons were calculated for each slice and 513 averaged across genotype, revealing a reduced degree of similarity in PC ensembles during SWRs in

bioRxiv preprint doi: https://doi.org/10.1101/2020.02.21.959676; this version posted May 14, 2020. The copyright holder for this preprint (which was not certified by peer review) is the author/funder, who has granted bioRxiv a license to display the preprint in perpetuity. It is made available under aCC-BY-NC-ND 4.0 International license.

514 5xFAD, as compared to control slices ($F_{(1,4100)}$ = 85.6, p < 10^{-15}; 2-way ANOVA; Fig. 3K), though with no
515 bins surviving multiple comparisons. This suggests there may be an increased repertoire of ensembles
516 in 5xFAD slices. The similarity between sPCs and all other PCs was reduced ($F_{(1,3600)}$ = 25.2, p = 5.5 ×
517 10^{-7}; 2-way ANOVA; Fig. 3L), with similarities between 0.1 – 0.15 surviving multiple comparisons, as was
518 the similarity between dPCs and all other PCs ($F_{(1,3800)}$ = 15.88, p = 6.9 × 10^{-5}; 2-way ANOVA; Fig. 3M),
519 suggesting aberrant cell participation may be disrupting ensembles.

520 ***Pyramidal cell spiking is relatively unchanged in 5xFAD mice***

521 To test more directly if pyramidal cell activity was altered, GCaMP6f+ sPCs (n_{sPC} = 13 CT, 9 5xFAD)
522 and dPCs (n_{dPC} = 26 CT, 35 5xFAD) were targeted for loose cell-attached recordings (Fig. 4A). Most cells
523 (n_{PC} = 39 CT, 39 5xFAD) were from 5xFAD;Thy1-GCaMP6f and Thy1-GCaMP6f littermate controls. A
524 small number (n_{sPC} = 1, n_{dPC} = 4) were from 5xFAD;Thy1-GCaMP6f;PV^{Cre}/+;tdTom/+ mice, which labeled
525 both excitatory PCs in green and inhibitory PV cells in red. Spikes and bursts (three or more spikes each
526 within 60 ms) were delineated as spontaneous or SWR-coincident (Fig. 4B). Consistent with prior studies
527 (Mizuseki and Buzsáki, 2013), the distribution of spike rates was lognormal for both sPCs and dPCs.
528 Both sPCs (Fig. 4C) and dPCs (Fig. 4D) increased their spike rate during SWRs, with a significant effect
529 of spontaneous/SWR time period (sPCs: $F_{(1,20)}$ = 11.0, p = 0.0034; dPCs: $F_{(1,59)}$ = 18.5, p = 6.4 × 10^{-5}; 2-
530 way RM ANOVAs, ART—zero-values preclude LT), with only sPCs/dPCs from 5xFAD mice showing a
531 significant spike rate increase when correcting for multiple comparisons (sPCs: p = 0.272 (CT), p = 0.023
532 (5xFAD); dPCs: p = 0.085 (CT), p = 0.00013 (5xFAD); Wilcoxon *post hoc*, ŠC). sPCs displayed a
533 significant genotype difference ($F_{(1,20)}$ = 4.64, p = 0.044), and interaction of genotype × period ($F_{(1,20)}$ =
534 5.59, p = 0.028), though neither the spontaneous nor SWR spike rate survived multiple comparisons
535 (Spont: p = 0.934, SWR: p = 0.301; Mann-Whitney *post hoc*, ŠC). In contrast, dPCs displayed no
536 genotype difference ($F_{(1,59)}$ = 0.914, p = 0.343), nor interaction of genotype × period ($F_{(1,59)}$ = 1.803, p =
537 0.184).

538 To examine spike rate in more detail around SWR events, the peri-SWR spike probability was
539 averaged across all cells within each genotype, showing an increased spiking probability in 5xFAD sPCs
540 ($F_{(1,2000)}$ = 37.73, p = 9.8 × 10^{-10}; 2-way ANOVA; Fig. 4E), with significant differences when correcting for

bioRxiv preprint doi: https://doi.org/10.1101/2020.02.21.959676; this version posted May 14, 2020. The copyright holder for this preprint (which was not certified by peer review) is the author/funder, who has granted bioRxiv a license to display the preprint in perpetuity. It is made available under aCC-BY-NC-ND 4.0 International license.

541 multiple comparisons from -4 ms to +8 ms around the SWR peak ($p < 0.01$, ŠC). In contrast, the dPC
542 spike probability did not differ between genotype ($F_{(1,5900)} = 2.38$, $p = 0.123$; 2-way ANOVA; Fig. 4F).
543 There was no difference in the rate of spike bursts (3 or more spikes each within 60 ms) between
544 genotype ($F_{(1,79)} = 1.00$, $p = 0.319$; 2-way ANOVA, ART; Fig. 4G) or PC type ($F_{(1,79)} = 2.37$, $p = 0.127$).
545 There was a tendency for a significant effect of genotype on the intra-burst interval ($F_{(1,77)} = 3.26$, $p =$
546 0.075; 2-way ANOVA, ART; Fig. 4H), with dPCs spiking somewhat faster from 14.4 ± 1.6 to 11.1 ± 0.8
547 ms ($p = 0.045$, ŠC) and with no change for sPCs ($p = 0.997$, ŠC). The percentage of cells with bursts did
548 not differ between genotype (97.6% CT, 96.1% 5xFAD; $\chi^2_{(3)} = 0.158$, $p = 0.691$; Chi-Squared Test). In
549 particular, 100% of sPCs had at least one burst in both CT and 5xFAD mice, an important consideration
550 given prior work indicating dPCs burst more than sPCs (Mizuseki et al., 2011). As we only targeted cells
551 with visible calcium transients for localization under confocal microscopy, it is possible the population of
552 sPCs and dPCs studied are a more highly active subset of all PCs. We also examined if the fractional
553 participation of PCs in SWRs differed, quantified as the fraction of spikes that occurred during SWRs
554 (Fig. 4I), and the fraction of SWRs that had one or more spikes (Fig. 4J). There was a tendency for an
555 effect of genotype for both endpoints ($F_{(1,79)} = 3.90$, $p = 0.052$; $F_{(1,79)} = 3.11$, $p = 0.082$; 2-way ANOVA,
556 ART), though with neither cell type surviving multiple comparisons (Fig. 4I-J).

557 Finally, we examined the phase-locking of spikes in both the slow gamma and ripple ranges (Fig.
558 4K). Phase-locking of PCs to the trough of ripples has been widely reported *in vivo* (Ylinen et al., 1995;
559 Csicsvari et al., 1999; Le Van Quyen et al., 2008). Additionally, phase-locking of spikes to SWR-nested
560 slow gamma has been reported to be reduced in 5xFAD mice (Iaccarino et al., 2016). We observed that
561 sPCs showed broad phase preference in the gamma range, with averages following the trough at 223°
562 for controls ($Z = 0.365$, $p = 0.706$; Raleigh Test), and following the peak at 63° in 5xFAD mice ($Z = 1.88$,
563 $p = 0.154$; Raleigh Test), with no significant genotype difference ($P = 2.86$, $p = 0.091$, Circular-Median
564 Test; Fig. 4L). In contrast, control dPCs were significantly phase-locked at 143° (110°-177° 95%; $Z =$
565 5.79, $p = 0.0023$; Raleigh Test), while 5xFAD dPCs showed a broader phase preference with a mean of
566 177° (110°-245° 95%; $Z = 2.25$, $p = 0.105$; Raleigh Test), and no significant genotype difference ($P =$
567 0.147, $p = 0.701$, Circular-Median Test; Fig. 4M). In the ripple range cells displayed broad phase

bioRxiv preprint doi: https://doi.org/10.1101/2020.02.21.959676; this version posted May 14, 2020. The copyright holder for this preprint (which was not certified by peer review) is the author/funder, who has granted bioRxiv a license to display the preprint in perpetuity. It is made available under aCC-BY-NC-ND 4.0 International license.

568 preference, with neither sPCs Z = 0.355, p = 0.712; Z = 1.58, p = 0.212; Raleigh Test; Fig. 4N) nor dPCs
569 (Z = 0.981, p = 0.340; 5xFAD: Z = 1.09, p = 0.339; Raleigh Test; Fig. 4O) significantly phase-locked, nor
570 different between genotypes (sPC: P = 0.254, p = 0.614; dPC: P = 0.528, p = 0.467; Circular-Median
571 Test). However, in control dPCs, the mean phase at the trough of 191° more closely matches prior *in*
572 *vivo* findings than for 5xFAD mice, with a mean phase of 224° following the trough (Fig. 4O). These
573 results indicate that spike-phase coupling may be impaired in 5xFAD mice, though the lack of significant
574 ripple phase-locking for either genotype suggests there are limitations to this analysis in our slice
575 preparation, as this finding differs from the robust ripple phase-locking observed *in vivo* (Ylinen et al.,
576 1995; Csicsvari et al., 1999; Le Van Quyen et al., 2008). One difference between our study and prior *in*
577 *vivo* recordings is that the spikes and LFP were recorded from different electrodes, while *in vivo* LFP and
578 spikes are typically recorded from the same set of channels. As ripples are highly localized events, the
579 distance between electrodes may confound spatial phase locking. Taken together with the Ca^{2+} imaging
580 data, these results indicate relatively minor alterations to the spiking activity of PCs in 5xFAD slices.
581 However, the large variability in spiking rate may mask small differences in activity.

582 ***Pyramidal cells receive increased synaptic E/I ratio***

583 Following the cell-attached recording of PC spiking activity, the electrode was replaced with one
584 containing a Cesium-based internal solution and the same cell targeted for a whole-cell voltage-clamp
585 recording to detect excitatory and inhibitory post-synaptic currents (EPSCs and IPSCs) at -70 mV (n_{sPC}
586 = 7 CT, 5 5xFAD; n_{dPC} = 12 CT, 9 5xFAD; Fig. 5A-B) and 0 mV (n_{sPC} = 7 CT, 5 5xFAD; n_{dPC} = 14 CT, 11
587 5xFAD; Fig. 5C-D), respectively. Events were sorted as spontaneous (sEPSCs/sIPSCs) or SWR-
588 coincident (swrEPSCs/swrIPSCs). sEPSC frequency and amplitude were unchanged across genotype
589 (Freq: $F_{(1,29)}$ = 0.296, p = 0.591; Fig. 5E; Amp: $F_{(1,29)}$ = 2.26, p = 0.143; Fig. 5F; 2-way ANOVA, LT), as
590 were the kinetics of sEPSCs (Rise tau: $F_{(1,29)}$ = 0.540, p = 0.468; Fig. 5G; Decay tau: $F_{(1,29)}$ = 0.268, p =
591 0.608; Fig. 5H; 2-way ANOVA). The excitatory charge during spontaneous periods (sEPSQ) was also
592 unchanged across genotype ($F_{(1,29)}$ = 0.835, p = 0.369; 2-way ANOVA, LT; Fig. 5I). However, there was
593 a significant effect of genotype on the excitatory charge during SWRs (swrEPSQ) ($F_{(1,29)}$ = 6.56, p =
594 0.016; 2-way ANOVA, LT; Fig. 5J), with dPCs seeing a 114 ± 41% increase (p = 0.043, ŠC), while sPCs

bioRxiv preprint doi: https://doi.org/10.1101/2020.02.21.959676; this version posted May 14, 2020. The copyright holder for this preprint (which was not certified by peer review) is the author/funder, who has granted bioRxiv a license to display the preprint in perpetuity. It is made available under aCC-BY-NC-ND 4.0 International license.

595 were not significantly different ($p = 0.368$, ŠC). Considering we observed that SWRs in 5xFAD mice were
596 larger in amplitude with more total PCs active, this was not an altogether surprising result. This increase
597 indicates that the enlarged SWRs were accompanied with increased excitatory synaptic activity, likely
598 originating from the CA3 region. The lack of any increase in spontaneous excitatory activity is also
599 consistent with our cell-attached results showing that at least locally in CA1, both sPCs and dPCs had
600 no changes in firing rate during spontaneous periods (Fig. 4C-D). Together these results indicate that
601 spontaneous excitatory synaptic input is unchanged, but increased during SWRs in 5xFAD mice,
602 particularly for dPCs, consistent with expectations from our LFP experiments.

603 In contrast, for sIPSCs, there was an effect of genotype on the frequency ($F_{(1,33)} = 9.38$, $p = 0.0043$;
604 2-way ANOVA, LT; Fig. 5K), as well as an effect of PC type ($F_{(1,33)} = 8.19$, $p = 0.0073$), with sPCs seeing
605 a preferential 52 ± 10% decrease ($p = 0.049$, ŠC), while dPCs were unchanged ($p = 0.466$, ŠC). There
606 was a tendency for an effect of genotype on the amplitude of sIPSCs ($F_{(1,33)} = 3.40$, $p = 0.074$; 2-way
607 ANOVA, LT; Fig. 5L), and no effect for the rise tau ($F_{(1,33)} = 1.73$, $p = 0.197$; 2-way ANOVA; Fig. 5M).
608 However the decay tau of sIPSCs saw an effect of genotype ($F_{(1,33)} = 9.36$, $p = 0.0044$; 2-way ANOVA;
609 Fig. 5N), cell type ($F_{(1,33)} = 10.7$, $p = 0.0025$), and interaction of genotype × cell type ($F_{(1,33)} = 7.61$, $p =$
610 0.0094), with sPCs from 5xFAD mice displaying a 5 ms longer decay than control sPCs ($p = 0.030$, ŠC)
611 and dPCs ($p = 0.00072$, ŠC). This specific alteration prompted us to examine in more detail the
612 distribution of sIPSCs. For each cell, the cumulative distribution function of all events was calculated and
613 averaged across cells. This analysis revealed for sPCs a significantly lower sIPSC amplitude ($F_{(1,1000)} =$
614 39.8, $p = 4.2 \times 10^{-15}$; 2-way ANOVA; Fig. 5O, upper) and greater decay tau ($F_{(1,1000)} = 469$, $p < 10^{-15}$; 2-
615 way ANOVA; Fig. 5P, upper), with events of amplitude 10 - 65 pA and decay tau 9 - 22 ms surviving
616 multiple comparisons. This suggests that for sPCs, fast and high amplitude inhibitory input, typically
617 attributed to fast-spiking cells, is preferentially reduced. In contrast, dPCs saw no significant range of bins
618 survive multiple comparisons (Fig. O-P, lower). This analysis was performed for all sEPSC and sIPSC
619 end-points, and no other end-points saw significant genotype differences surviving multiple comparisons.

620 The normalized inhibitory charge during spontaneous periods (sIPSQ) was also preferentially
621 reduced for 5xFAD sPCs (Genotype Effect: $F_{(1,33)} = 10.3$, $p = 0.0029$; 2-way ANOVA, LT; sPC: $p = 0.044$,

bioRxiv preprint doi: https://doi.org/10.1101/2020.02.21.959676; this version posted May 14, 2020. The copyright holder for this preprint (which was not certified by peer review) is the author/funder, who has granted bioRxiv a license to display the preprint in perpetuity. It is made available under aCC-BY-NC-ND 4.0 International license.

622 dPC: p = 0.331, ŠC; Fig. 5Q). During SWRs, the total inhibitory charge (swrIPSQ) was differentially
623 altered between cell types, with a significant interaction of genotype and cell type ($F_{(1,33)}$ = 7.14, p =
624 0.0116; 2-way ANOVA, LT; Fig. 5R), a non-significant reduction for sPCs (p = 0.294, ŠC) and a significant
625 increase for dPCs (p = 0.022, ŠC). These results suggest a selective impairment in inhibition in sPCs
626 that is not seen in dPCs. Despite the observed increase in SWR activity in 5xFAD mice, the inhibition did
627 not scale proportionally with the increased excitation, thus shifting the synaptic E/I balance. We assessed
628 this for both spontaneous and SWR-driven currents. During spontaneous periods, there was a significant
629 effect of genotype on the E/I ratio, defined as the ratio of sEPSQ/sIPSQ ($F_{(1,27)}$ = 14.7, p = 0.00069; 2-
630 way ANOVA; Fig. S), as well as an effect of cell type ($F_{(1,27)}$ = 7.39, p = 0.0113). Both sPCs and dPCs
631 saw an increase (sPC: p = 0.055, dPC: p = 0.049, ŠC). During SWRs, the synaptic E/I ratio
632 (swrEPSQ/swrIPSQ) was affected by both genotype ($F_{(1,27)}$ = 7.59, p = 0.0104; 2-way ANOVA; Fig. R)
633 and a genotype x cell type interaction ($F_{(1,27)}$ = 5.12, p = 0.0319), but only in sPCs was there an increase
634 (sPC: p = 0.048, dPC: p = 0.877). To examine the temporal progression of synaptic input during SWRs,
635 we calculated the EPSQ and IPSQ in a sliding 100 ms window across the SWR peak (Fig. 5U-V), from
636 which a time course of the synaptic E/I ratio could be determined (Fig. 5W-X). While for both the EPSQ
637 and IPSQ there was a significant effect of genotype for sPCs (EPSQ: $F_{(1,1000)}$ = 184, $p < 10^{-15}$; IPSQ:
638 $F_{(1,1000)}$ = 129, $p < 10^{-15}$; 2-way ANOVA; Fig. 5U) and dPCs (EPSQ: $F_{(1,1900)}$ = 295, $p < 10^{-15}$; IPSQ: $F_{(1,2300)}$
639 = 708, $p < 10^{-15}$; 2-way ANOVA; Fig. 5V), only for the IPSQ in dPCs did individual bins from -18 to +62
640 ms (relative to the SWR peak) survive multiple comparisons. The ratio of the EPSQ/IPSQ time course
641 revealed a significant effect of genotype for both sPCs ($F_{(1,1000)}$ = 159, $p < 10^{-15}$; 2-way ANOVA; Fig. 5W)
642 and dPCs ($F_{(1,1800)}$ = 24.3, p = 9.1×10^{-7}; 2-way ANOVA; Fig. 5X). For both sPCs and dPCs there was an
643 early peak in the synaptic E/I ratio for 5xFAD mice that was not present in controls (Fig. 5W-X), which
644 can be attributed to a build-up in excitation with a delayed increase in inhibition. Only for dPCs did
645 individual bins from -70 to -60 ms survive multiple comparisons, in part likely due to the greater sampling
646 of dPCs.

bioRxiv preprint doi: https://doi.org/10.1101/2020.02.21.959676; this version posted May 14, 2020. The copyright holder for this preprint (which was not certified by peer review) is the author/funder, who has granted bioRxiv a license to display the preprint in perpetuity. It is made available under aCC-BY-NC-ND 4.0 International license.

647 ***PV basket cells have selectively reduced spiking***

648 While there are numerous inhibitory cell sub-types in the CA1 region that could underlie a shift in
649 E/I synaptic input to PCs (Pelkey et al., 2017), we focused on parvalbumin-expressing (PV) interneurons,
650 as they are the most highly active during SWR events (Somogyi et al., 2014). We performed cell-attached
651 recordings in 5xFAD/+;PV^{Cre}/+;tdTom/+ and PV^{Cre}/+;tdTom/+ littermate controls (n_{cell} = 13 CT, 18 5xFAD)
652 (Fig. 6A). Cells were also recorded from 5xFAD;Thy1-GCaMP6f;PV^{Cre}/+;tdTom/+ and Thy1-
653 GCaMP6f;PV^{Cre}/+;tdTom/+ littermate controls (n_{cell} = 11 CT, 14 5xFAD), which were pooled together.
654 One complication with the PV cell population is that there are at least three distinct sub-types within CA1
655 *str. pyr.*, which vary in function and axonal target: basket cells (PVBCs), which target perisomatic regions
656 of PCs, bistratified cells (PVBSCs), which target both apical and basal dendrites of PCs, and axo-axonic
657 cells (PVAACs), which selectively target the axon initial segment (AIS) (Fig. 6B). To distinguish these,
658 we morphologically reconstructed the cells *post hoc* after filling with biocytin in whole-cell configuration
659 (Fig. 6C) and sorted them by axonal target. Of the total reconstructed cells (n_{cell} = 24 CT, 32 5xFAD),
660 PVBSCs (Fig. 6C.2) were easily distinguished from both PVBCs (Fig. 6C.1) and PVAACs (Fig. 6C.3),
661 with their axonal arbor avoiding *str. pyramidale* (n_{PVBSC} = 5 CT, 10 5xFAD). While PVBCs and PVAACs
662 have overlapping axonal targets, some PVBCs were easily distinguished with axonal terminals directly
663 targeting PC somas as visualized through the PV^{Cre}-tdTom and/or Thy1-GCaMP6f fluorescence (n_{PVBC} =
664 9 CT, 9 5xFAD). Likewise, some PVAACs exhibited the characteristic "chandelier" phenotype and lack
665 of somatic targeting (n_{PVAAC} = 4 CT, 4 5xFAD). However, there were some cells with ambiguous
666 PVBC/PVAAC morphology based solely on axonal targets (n_{cell} = 6 CT, 9 5xFAD). To sort these cells,
667 we examined the spike rate. Both PVBCs and PVBSCs are known to strongly increase their spike rate
668 during SWRs (Lapray et al., 2012; Katona et al., 2014), while the PVAAC spike rate does not increase
669 (Viney et al., 2013). Thus, for cells with ambiguous PVBC/PVAAC morphology, those with a spike rate
670 increase during SWRs (53 ± 11 Hz) were sorted as putative PVBCs, while those with no increase (0.6 ±
671 0.6 Hz) were sorted as putative PVAACs. In a subset of 14 slices (5 CT, 9 5xFAD from n_{mice} = 4 CT, 5
672 5xFAD), we additionally stained for Ankyrin G, which labels the AIS, and confirmed colocalization with
673 two putative PVAACs (Fig. 6C.4). Based on this sorting methodology, we identified a total of n_{PVBC} = 13

bioRxiv preprint doi: https://doi.org/10.1101/2020.02.21.959676; this version posted May 14, 2020. The copyright holder for this preprint (which was not certified by peer review) is the author/funder, who has granted bioRxiv a license to display the preprint in perpetuity. It is made available under aCC-BY-NC-ND 4.0 International license.

674 CT, 16 5xFAD, n_{PVBSC} = 5 CT, 10 5xFAD, and n_{PVAAC} = 6 CT, 6 5xFAD. The proportion of cells did not
675 significantly differ from prior published findings of 60% PVBC, 25% PVBSC, 15% PVAAC in CA1 *str. pyr.*
676 ($\chi^2_{(2)}$ = 0.754, p = 0.686) (Baude et al., 2007), and did not significantly differ between genotype ($\chi^2_{(2)}$ =
677 1.09, p = 0.580; Fig. 6D).

678 Based on these delineations, we performed PV cell-attached + LFP recordings in control and
679 5xFAD mice for the identified populations of PVBCs (Fig. 7A.1), PVBSCs (Fig. 7A.2) and PVAACs (Fig.
680 7A.3). We observed an effect of genotype on PVBC spike rate ($F_{(1,27)}$ = 10.4, p = 0.0033; 2-way RM
681 ANOVA, ART; Fig. 7B.1), with a selective and robust reduction during SWR periods, from 62.9 ± 10.6 Hz
682 to 34.0 ± 6.2 Hz (p = 0.044; Mann-Whitney *post hoc*, ŠC), whereas the spontaneous spike rate did not
683 significantly differ (p = 0.209; Mann-Whitney *post hoc*, ŠC). In contrast, there was no effect of genotype
684 on the spike rate of PVBSCs ($F_{(1,13)}$ = 1.35, p = 0.267; 2-way RM ANOVA, ART; Fig. 7B.2) or PVAACs
685 ($F_{(1,10)}$ = 3.83, p = 0.079; 2-way RM ANOVA, ART; Fig. 7B.3). As expected from the cell-sorting
686 methodology, spike rates increased during SWRS for PVBCs, with an effect of period ($F_{(1,27)}$ = 179, p =
687 1.9×10^{-13}; Fig. 7B.1), and increases of 5.6 ± 1.2 fold in control (p = 0.00049; Wilcoxon *post hoc,* ŠC)
688 and 5.9 ± 2.4 fold in 5xFAD mice (p = 0.00012; Wilcoxon *post hoc,* ŠC). Additionally, there was an
689 interaction of genotype × period ($F_{(1,27)}$ = 16.8, p = 0.00034), indicating that PVBC modulation of spiking
690 during SWRs differed between genotype. Similarly, there was an effect of period for PVBSCs ($F_{(1,13)}$ =
691 30.6, p = 9.7×10^{-5}; Fig. 7B.2), with a non-significant 4.4 ± 1.2 fold increase in control (p = 0.121; Wilcoxon
692 *post hoc*, ŠC) and a 6.8 ± 5.0 fold increase in 5xFAD mice (p = 0.019; Wilcoxon *post hoc*, ŠC), and no
693 interaction of genotype × period ($F_{(1,13)}$ = 2.56, p = 0.133). While PVAACs did see an effect of period
694 ($F_{(1,10)}$ = 16.7, p = 0.0022; Fig. 7B.3), neither in control nor 5xFAD mice was the increase significant (CT:
695 1.0 ± 0.4 fold, p = 0.527, 5xFAD: 2.4 ± 0.8 fold, p = 0.062; Wilcoxon *post hoc*, ŠC), nor was there an
696 interaction of genotype × period ($F_{(1,10)}$ = 3.21, p = 0.104). However, the low number of PVAACs recorded
697 from may mask small alterations in this cell population.

698 The peri-SWR spike probability revealed that in 5xFAD mice, PVBCs spikes fell in a significantly
699 narrower window (Fig. 7C.1), with a reduced full-width half-maximum value from 44 ± 19 ms to 18 ± 5
700 ms, and a significant effect of genotype when analyzed via 2-way ANOVA ($F_{(1,2700)}$ = 267, $p < 10^{-15}$), with

bioRxiv preprint doi: https://doi.org/10.1101/2020.02.21.959676; this version posted May 14, 2020. The copyright holder for this preprint (which was not certified by peer review) is the author/funder, who has granted bioRxiv a license to display the preprint in perpetuity. It is made available under aCC-BY-NC-ND 4.0 International license.

701 bins from -20 to -16 ms and 0 to +20 ms relative to the SWR peak surviving multiple comparisons.
702 Intriguingly, this narrower window of spiking in 5xFAD mice was accompanied by shorter duration SWRs
703 (Fig. 2D), suggesting the activity of these cells is critical for normal ripple progression. In contrast,
704 PVBSCs appeared to increase their firing after the SWR peak in 5xFAD mice (Fig. 7C.2), perhaps playing
705 a compensatory role, with a significant effect of genotype ($F_{(1,1300)} = 33.9$, $p = 7.3 \times 10^{-9}$; 2-way ANOVA).
706 PVAACs appeared to have decreased probability of spiking in 5xFAD mice, particularly before the SWR
707 peak (Fig. 7C.3), with a significant effect of genotype ($F_{(1,1000)} = 30.15$, $p = 5.1 \times 10^{-8}$; 2-way ANOVA).
708 However, unlike PVBCs, neither PVBSCs nor PVAACs showed significant genotype differences when
709 corrected for multiple comparisons (Fig. 7C).

710 Considering the rate of bursts, defined as three or more spikes each within 40 ms, there was a
711 tendency for a reduction for PVBCs (U = 60, p = 0.056; Mann-Whitney; Fig. 7D.1) and no change for
712 PVBSCs (U = 22.5, p = 0.793; Mann-Whitney; Fig. 7D.2) or PVAACs (U = 24, p > 0.999; Mann-Whitney;
713 Fig. 7D.3). No differences were observed in the proportion of cells that exhibited bursts for PVBCs (100%
714 CT, 93.8% 5xFAD; $\chi^2_{(1)} = 0.842$, p = 0.359; χ^2 Test), PVBSCs (80.0% CT, 90.0% 5xFAD; $\chi^2_{(1)} = 0.288$, p
715 = 0.591), or PVAACs (50.0% CT, 83.3% 5xFAD; $\chi^2_{(1)} = 1.500$, p = 0.221). The fraction of SWRs that
716 coincided with a PV spike was no different between genotypes for PVBCs (U = 72, p = 0.170; Mann-
717 Whitney; Fig. 7E.1), PVBSCs (U = 21, p = 0.655; Mann-Whitney; Fig. 7E.2), or PVAACs (U = 6, p = 0.065;
718 Mann-Whitney; Fig. 7E.3). However in PVBCs, the fraction of SWRs that coincided with a PV burst was
719 significantly reduced from 65.4 ± 8.5% to 32.9 ± 8.5% (U = 53, p = 0.025; Mann-Whitney; Fig. 7F.1), while
720 there was no genotype difference for PVBSCs (U = 16.5, p = 0.323; Mann-Whitney; Fig. 7F.2) or PVAACs
721 (U = 10.5, p = 0.182; Mann-Whitney; Fig. 7F.3).

722 We also examined the spike phase-locking of these three PV cell types, as these have been
723 carefully studied *in vivo* for theta (8-12 Hz, during mobility) and ripple oscillations (Varga et al., 2014).
724 The precise temporal ordering of PV cell sub-types during network oscillations has been proposed to play
725 a critical role in the spatiotemporal control of PCs. During ripples, PVBCs have been observed to fire just
726 after the trough of the ripple, followed by PVBSCs and then PVAACs. Less studied is the phase-locking
727 of PV cells during SWR-nested slow gamma oscillations, which we examined as we observed alterations

bioRxiv preprint doi: https://doi.org/10.1101/2020.02.21.959676; this version posted May 14, 2020. The copyright holder for this preprint (which was not certified by peer review) is the author/funder, who has granted bioRxiv a license to display the preprint in perpetuity. It is made available under aCC-BY-NC-ND 4.0 International license.

728 in this endpoint for the PC population (Fig. 4M). We found significant gamma phase-locking of PVBCs
729 for 5xFAD mice at 273° (247°-298° 95%; Z = 7.94, p = 0.00012; Raleigh's test), with broader phase
730 preference in control mice (Z = 2.48, p = 0.082; Raleigh's test), and with no difference in median phase
731 angle (P = 0.144, p = 0.705; Circular median test; Fig. 7G.1). PVBSCs were similarly gamma phase-
732 locked for 5xFAD mice at 292° (249°-336° 95%; Z = 3.54, p = 0.024; Raleigh's test), with broader phase
733 preference in control mice (Z = 1.57, p = 0.216; Raleigh's test), and with no difference in median phase
734 angle (P = 0.311, p = 0.577; Circular median test; Fig. 7G.2). In contrast, in PVAACs we observed phase-
735 locking in control mice at 246° (224°-368° 95%; Z = 4.43, p = 0.005; Raleigh's test), with broader phase
736 preference in 5xFAD mice (Z = 0.913, p = 0.421; Raleigh's test), and with a tendency for a difference in
737 median phase angle (P = 3.60, p = 0.058; Circular median test; Fig. 7G.3). While the precise significance
738 of gamma phase-locking has yet to be demonstrated, these genotype differences point to a temporal
739 disordering of PV cell inhibition.

740 Within the ripple range, in PVBCs, there was a significant phase-locking in control mice at 228°
741 (198°-259° 95%; Z = 6.01, p = 0.0014; Raleigh's test), and in 5xFAD mice at 208° (186°-231° 95%; Z =
742 9.35, p = 1.7×10^{-5}; Raleigh's test), with no significant genotype difference ($F_{(1,27)}$ = 1.34, p = 0.258;
743 Watson-Williams; Fig. 7H.1). These values are in line with prior *in vivo* studies, where 0° in our study was
744 defined as the peak of the ripple cycle and 180° as the trough. PVBSCs exhibited more varied phase-
745 locking in the ripple range, although the average angles are in line with *in vivo* studies (CT: 241°, Z =
746 1.63, p = 0.202; 5xFAD: 225°, Z = 1.33, p = 0.270; Raleigh's test; Fig. 7H.2). PVAACs exhibited ripple
747 phase preference for control mice at 257° (219°-296° 95%; Z = 3.75, p = 0.0015; Raleigh's test), in line
748 with *in vivo* studies. However, in 5xFAD mice, PVAACs spiked earlier, at 204° (164°-245° 95%; Z = 3.54,
749 p = 0.0020; Raleigh's test), with a significant genotype difference in mean phase angle ($F_{(1,9)}$ = 5.68, p =
750 0.044; Watson-Williams; Fig. 7H.3). Although we observed no significant change in PVAAC spike rate,
751 this disruption in temporal ordering may still have downstream network consequences.

752 ***PV basket cells have selective decrease in excitatory synaptic drive and decreased E/I ratio***

753 Following cell-attached recording of spiking activity, the electrode was replaced with a Cesium
754 internal and the same PV cell was targeted for a whole-cell voltage-clamp recording. EPSCs were

bioRxiv preprint doi: https://doi.org/10.1101/2020.02.21.959676; this version posted May 14, 2020. The copyright holder for this preprint (which was not certified by peer review) is the author/funder, who has granted bioRxiv a license to display the preprint in perpetuity. It is made available under aCC-BY-NC-ND 4.0 International license.

755 recorded at -70 mV for PVBCs (n_{PVBC} = 12 CT, 16 5xFAD; Fig. 8A.1), PVBSCs (n_{PVBSC} = 4 CT, 6 5xFAD;
756 Fig. 8A.2), and PVAACs (n_{PVAAC} = 5 CT, 6 5xFAD; Fig. 8A.3). None of the three PV cell subtypes had
757 any change in spontaneous sEPSC frequency (PVBC: $t_{(26)} = 1.30$, $p = 0.206$; PVBSC: $t_{(8)} = 0.990$, $p =$
758 0.351; PVAAC: $t_{(9)} = 0.129$, $p = 0.900$; unpaired t-tests), or amplitude (PVBC: $t_{(26)} = 0.545$, $p = 0.591$;
759 PVBSC: $t_{(8)} = 0.058$, $p = 0.956$; PVAAC: $t_{(9)} = 2.11$, $p = 0.064$; unpaired t-tests; Fig. 8B.1-3). The kinetics
760 of sEPSCs in 5xFAD PVBCs were altered however, with a similar rise tau ($t_{(26)} = 0.307$, $p = 0.761$;
761 unpaired t-test), but a reduction in the decay tau ($t_{(26)} = 2.41$, $p = 0.024$; unpaired t-test; Fig. 8C.1). There
762 were no changes to sEPSC kinetics in PVBSCs (Rise: $t_{(8)} = 0.671$, $p = 0.521$; Decay: $t_{(8)} = 1.02$, $p = 0.340$;
763 Fig. 8C.2) or PVAACs (Rise: $t_{(9)} = 0.857$, $p = 0.414$; Decay: $t_{(9)} = 1.79$, $p = 0.107$; Fig. 8C.3). To examine
764 the decreased sEPSC decay tau in PVBCs, the cumulative distribution function of all sEPSCs was
765 calculated and averaged across cells, revealing an effect of genotype ($F_{(1,2500)} = 2165$, $p < 10^{-15}$; 2-way
766 ANOVA; Fig. 8D), with events of decay tau 1 - 7 ms surviving multiple comparisons. This decrease in
767 decay tau was somewhat unexpected, considering that in PV cells, neuronal pentraxins are associated
768 with an acquisition of GluA4 subunits which speeds up the kinetics of AMPA receptor mediated EPSCs
769 (Pelkey et al., 2015). Both pentraxins and GluA4 are selectively reduced in human Alzheimer's patients
770 (Xiao et al., 2017), suggesting that in AD, a longer decay of AMPA-mediated EPSCs may underlie PV
771 cell dysfunction. Our results indicate that in 3 mo 5xFAD mice, this does not appear to be a prominent
772 mechanism.

773 During SWRs, PVBCs from 5xFAD mice saw a 50.1 ± 10.7% reduction in the swrEPSQ, the total
774 excitatory synaptic charge in a 100 ms window centered around the SWR peak ($t_{(26)} = 3.20$, $p = 0.0036$,
775 unpaired t-test; Fig. 8E.1), whereas there was no change for PVBSCs ($t_{(8)} = 0.997$, $p = 0.348$; unpaired
776 t-test; Fig. 8E.2) or PVAACs ($t_{(9)} = 1.63$, $p = 0.139$; unpaired t-test; Fig. 8D.3). In a subset of cells (n_{PVBC}
777 = 8 CT, 8 5xFAD), we also recorded IPSCs at 0 mV (Fig. 8A.4 for PVBCs, IPSCs were not recorded in
778 every cell, thus there were insufficient numbers of PVBSCs and PVAACs for statistical analysis).
779 Spontaneous inhibitory input to PVBCs was unchanged, including sIPSC frequency ($t_{(14)} = 0.448$, $p =$
780 0.661; unpaired t-test), amplitude ($t_{(14)} = 0.339$, $p = 0.740$; unpaired t-test; Fig. 8B.4), and kinetics (Rise:
781 $t_{(14)} = 0.263$, $p = 0.796$; Decay: $t_{(14)} = 0.672$, $p = 0.513$; Fig. 8C.4). The total inhibitory charge during

bioRxiv preprint doi: https://doi.org/10.1101/2020.02.21.959676; this version posted May 14, 2020. The copyright holder for this preprint (which was not certified by peer review) is the author/funder, who has granted bioRxiv a license to display the preprint in perpetuity. It is made available under aCC-BY-NC-ND 4.0 International license.

782 SWRs, swrIPSQ, was also no different between genotype ($t_{(14)} = 0.0083$, $p = 0.994$; unpaired t-test; Fig.
783 E.4). This selective decrease in excitation to PVBCs during SWRs, in contrast to the observation in PCs
784 (Fig. 5J), resulted in a significant decrease in the synaptic E/I ratio during SWRs ($t_{(14)} = 2.70$, $p = 0.017$,
785 unpaired t-test), though not during spontaneous periods ($t_{(14)} = 0.929$, $p = 0.368$, unpaired t-test; Fig. 8F).
786 As with PCs, we examined the time course of synaptic charge during SWRs in PVBCs, and found a
787 significant effect of genotype on the excitatory charge ($F_{(1,2500)} = 664$, $p < 10^{-15}$; 2-way ANOVA), with bins
788 from -32 to +42 ms relative to the SWR peak surviving multiple comparisons (Fig. 8G). There was no
789 effect of genotype on inhibitory charge ($F_{(1,1400)} = 2.12$, $p = 0.145$, 2-way ANOVA; Fig. 8G). This resulted
790 in a significant effect of genotype on the E/I ratio ($F_{(1,1300)} = 339$, $p < 10^{-15}$, 2-way ANOVA), with an early
791 peak that survived multiple comparisons in control above 5xFAD cells from -66 to -58 ms relative to the
792 SWR peak (Fig. 8H), precisely the opposite effect observed in PCs (Fig. 5W-X)

793 Since we recorded the cell-attached spiking activity from the same PVBCs, we were next
794 interested if reduced SWR spike rate (Fig. 7B.1) was correlated with altered synaptic E/I ratio during
795 SWRs. We observed a moderate positive correlation for control PVBCs ($n_{PVBC} = 8$, $R^2 = 0.625$, $F_{(1,6)} =$
796 9.98, $p = 0.020$, Linear Regression), but no correlation between spike rate and E/I ratio for 5xFAD PVBCs
797 ($n_{PVBC} = 8$, $R^2 = 0.0092$, $F_{(1,6)} = 0.056$, $p = 0.822$; Fig. 8I), suggesting that not only is excitatory synaptic
798 input during SWRs reduced, potentially through altered PC-PVBC connectivity, but there are also deficits
799 in PVBC input-output function, consistent with prior studies of intrinsic PV cell dysfunction (Verret et al.,
800 2012).

bioRxiv preprint doi: https://doi.org/10.1101/2020.02.21.959676; this version posted May 14, 2020. The copyright holder for this preprint (which was not certified by peer review) is the author/funder, who has granted bioRxiv a license to display the preprint in perpetuity. It is made available under aCC-BY-NC-ND 4.0 International license.

801 **Discussion**

802 Here we identified a selective reduction in PVBC activity in a model of AD, while PVBSCs, PVAACs,
803 and excitatory PCs were relatively spared. By investigating the synaptic input and spike output of these
804 cell types, we present a careful description of hippocampal micro-circuitry alterations in early amyloid
805 pathology (Fig. 9) during activity critical for memory consolidation (i.e. SWRs). PVBCs displayed a
806 reduced synaptic E/I ratio during SWRs (Fig. 8F), driven by a reduction in excitatory synaptic input (Fig.
807 8E.1). PVBCs spiked less during SWRs (Fig. 7B.1), thus providing reduced inhibitory control to excitatory
808 PCs. In contrast, PCs displayed an increased synaptic E/I ratio (Fig. 5S-T), with differences between
809 superficial and deep PCs. sPCs saw a greater reduction in inhibitory input than dPCs (Fig. 5Q-R), and
810 also displayed an increased probability of spiking during SWRs (Fig. 4E-F). As the strong inhibition
811 PVBCs provide is critical for the selection of PC ensembles (Klausberger and Somogyi, 2008; Ellender
812 et al., 2010), this selective reduction may explain the enlarged PC ensembles (Fig. 3E), aberrant cellular
813 participation (Fig. 3L-M), and more frequent and larger amplitude SWRs in 5xFAD mice (Fig. 2C-D).
814 Intriguingly, the increase in SWRs appears detrimental, despite their role in memory consolidation, as we
815 also observed spatial memory deficits (Fig. 1C). Considering the surprising role SWRs play in down-
816 regulating synapses and reducing memory-irrelevant activity (Norimoto et al., 2018), these aberrant
817 SWRs may be interfering with memory-relevant reactivations. Several mechanisms likely contribute to
818 the increase in SWRs. The reduction of sIPSCs that sPCs receive between SWRs (Fig. 5K) may permit
819 the buildup of excitation necessary for SWR initiation. The decreased duration of SWRs (Fig. 2D) may
820 more quickly reset the system for subsequent events. A more complete description would also require
821 investigation of CA3 and CA2 micro-circuitry.

822 ***Hyperactivity and inhibitory disruption in Alzheimer's disease***

823 Our findings are consistent with growing evidence linking hyperactivity and Aβ aggregation (Zott et
824 al., 2018). Hippocampal hyperactivity is seen in mouse models of early amyloid pathology as increased
825 seizure risk (Palop et al., 2007) and enlarged ensemble activity (Busche et al., 2012). Our results extend
826 these findings to the study of SWRs. In addition, several studies have demonstrated that a preferential
827 disruption to inhibitory cells underlies hyperactivity (Verret et al., 2012; Hazra et al., 2013; Mahar et al.,

bioRxiv preprint doi: https://doi.org/10.1101/2020.02.21.959676; this version posted May 14, 2020. The copyright holder for this preprint (which was not certified by peer review) is the author/funder, who has granted bioRxiv a license to display the preprint in perpetuity. It is made available under aCC-BY-NC-ND 4.0 International license.

828 2016; Hijazi et al., 2019). In the clinical population, seizures are more prevalent and associated with
829 earlier onset of cognitive decline in amnestic MCI patients (Vossel et al., 2013). Additionally, task-related
830 engagement of the hippocampus, as tested via event-related fMRI, indicates hippocampal hyper-
831 activation in MCI patients relative to aged controls, while more progressed AD patients experience hypo-
832 activation (Dickerson et al., 2005; Pariente et al., 2005). These studies suggest our observed phenotype
833 may better model mild cognitive impairment rather than fully progressed AD.

834 ***Sharp wave ripple alterations in aging and disease***

835 In normal aging, SWR event and ripple frequency decrease (Wiegand et al., 2016; Cowen et al.,
836 2018), contrasting with the phenotype we observed in younger mice. While it is accepted that AD is
837 distinct from accelerated aging (Toepper, 2017), similar decreases in SWRs have been observed in aged
838 AD models. In an apoE-ε4 knockin model of sporadic AD, SWR event frequency and gamma power are
839 reduced in 12-18 mo mice (Gillespie et al., 2016; Jones et al., 2019). Similarly, in 9-12 mo TgF344-AD
840 rats, SWR event frequency, power, and gamma power are reduced (Stoiljkovic et al., 2018). In younger
841 adults the findings are somewhat mixed. As seen in a cohort of six 3 mo 5xFAD mice, SWR event
842 frequency and gamma power during non-theta periods are reduced (Iaccarino et al., 2016), the opposite
843 phenotype we observe in slice. In 2-4 mo rTg4510 mice, SWR event frequency is unchanged while
844 amplitude and ripple power are reduced (Ciupek et al., 2015). Another study has suggested a failure of
845 PC-PV circuits in amyloid pathology is due to regulation of the GluA4 AMPA receptor, resulting in more
846 frequent SWRs with reduced ripple frequency in 3-4 mo APP_{swe}/PS1ΔE9 mice (Xiao et al., 2017).
847 Propagation of SWRs also appears disrupted; 3 mo APP-PS1 mice show impaired propagation from CA3
848 to CA1 correlated with increased immunoreactivity for PV (Hollnagel et al., 2019).

849 One notable difference between our study and others is the acute slice versus *in vivo* preparation.
850 Slice electrophysiology permits a careful study of the synaptic inputs to different neuronal sub-types
851 during SWRs, an infeasible task *in vivo*. It is unknown if awake versus asleep SWR are differentially
852 affected in AD, and it is unclear which, if either, are better modeled in slice. The choice of AD model also
853 surely has implications. The 5xFAD model has several advantages over other mouse models in
854 replicating human disease: a high ratio of $A\beta_{42}$ over $A\beta_{40}$, memory impairment, and neurodegeneration

bioRxiv preprint doi: https://doi.org/10.1101/2020.02.21.959676; this version posted May 14, 2020. The copyright holder for this preprint (which was not certified by peer review) is the author/funder, who has granted bioRxiv a license to display the preprint in perpetuity. It is made available under aCC-BY-NC-ND 4.0 International license.

855 in later disease progression. However, it also has limitations. As with most AD models, it only models the
856 familial variant of the disease, while the sporadic variant accounts for most human cases. Moreover, the
857 presence of five APP/PS1 gene mutations would certainly never be observed in a patient. Another
858 disadvantage is APP overexpression, common to all first-generation transgenic models. Some have
859 noted electrophysiological alterations are more related to APP overexpression than Aβ aggregation (Born
860 et al., 2014). We attempted to address this by examining a 1 mo cohort (preceding plaque aggregation),
861 in which APP overexpression would still presumably have an effect, a cohort in which we observed no
862 alterations (Fig. 1C,2C). Fewer studies exist of second-generation APP knockin models which address
863 the APP overexpression problem, yet have less pronounced disease phenotypes (Sasaguri et al., 2017).
864 In one relevant study, sIPSC amplitude from putative PV cells is decreased in parietal cortex PCs from
865 18-20 mo App^{NL-F} mice, although synaptic E/I balance is unchanged (Chen et al., 2018). It will be critical
866 to study hippocampal network alterations, both at the level of the micro-circuit and behaving animal, in
867 novel AD mouse models with greater validity.

868 ***Potential mechanisms for PVBC deficit***

869 Several mechanisms may underlie PVBC dysfunction in amyloid pathology. Intrinsic factors
870 including downregulation of the voltage-gated $Na_{v1.1}$ channel can explain decreased PV cell excitability
871 and cortical network hyperactivity (Verret et al., 2012). It remains to be shown if different PV sub-types
872 are differentially affected, but according to the Allen Brain Institute Cell Types Database, all identified
873 murine PV clusters express the Scn1a gene encoding $Na_{v1.1}$ (Lein et al., 2007). Another potential
874 mechanism is loss of peri-neuronal nets (PNNs), part of the extracellular matrix surrounding soma and
875 proximal dendrites that preferentially ensheathe PV cells (Kwok et al., 2011; Sorg et al., 2016). The
876 function of PNN is incompletely understood, but both enhances PV cell excitability and activity (Slaker et
877 al., 2015; Balmer, 2016). In a prior study, we observed degradation of PNN increases SWR event
878 frequency by ~50% (Sun et al., 2017), a similar magnitude effect as the current study. Additionally, the
879 selective reduction of excitatory input to PV cells (Fig. 8E.1) is consistent with the decrease in miniature
880 EPSCs in PV cells in a brevican knockout, a major component of PNN (Favuzzi et al., 2017). Moreover,
881 PNN staining is reduced in 3 mo Tg2576 mice (Cattaud et al., 2018). PNNs are more selectively located

bioRxiv preprint doi: https://doi.org/10.1101/2020.02.21.959676; this version posted May 14, 2020. The copyright holder for this preprint (which was not certified by peer review) is the author/funder, who has granted bioRxiv a license to display the preprint in perpetuity. It is made available under aCC-BY-NC-ND 4.0 International license.

882 around PVBCs (>90%) than PVBSCs (25-50%) or PVAACs (<10%) (Yamada and Jinno, 2015),
883 potentially explaining the specificity we observe. However, our experiments would also be consistent with
884 upstream deficits in excitatory input to PV cells. In 4 mo Tg2576 mice, there is a preferential degeneration
885 of direct entorhinal input to CA1 PV cells; optogenetic restoration of this input rescues synaptic and spatial
886 learning deficits (Yang et al., 2016). The overall cause of disruption to PV cells is likely from several
887 contributing factors, and further studies are required to identify the most salient impairment, and thus the
888 most promising avenue for intervention.

889 ***Implications of PVBC specific deficit***

890 Here, we identified a preferential impairment in PVBC function, concurrent with altered network
891 activity. The selectivity of synaptic alterations in PVBCs suggest they may be a promising target for
892 intervention to restore hippocampal network activity in early amyloid pathology. Given the rapid evolution
893 of tools to manipulate activity in a cell-type specific manner, this finding is of particular importance
894 considering optogenetic (Iaccarino et al., 2016) and chemogenetic (Hijazi et al., 2019) approaches to
895 ameliorate memory decline in AD. A limitation of these strategies is that the PV^{Cre} driver will also target
896 PVBSCs and PVAACs, potentially leading to unintended off-target consequences in temporal
897 sequencing. Novel combinatorial approaches utilizing both Cre and Flp (He et al., 2016) provide a
898 promising avenue to selectively manipulate distinct neuronal sub-types. For example, the
899 $Nkx2.1^{CreER}$;LSL^{Flp} mouse would provide an efficient means to record PVAAC activity, in which we saw
900 small alterations that did not reach significance. In conclusion, this study investigated the synaptic input
901 and spiking output of distinct PC and PV cell-types within CA1 micro-circuitry over the course of SWR
902 events, providing insight into synaptic deficits in early amyloid pathology, and informing future attempts
903 to manipulate the hippocampal micro-circuit.

bioRxiv preprint doi: https://doi.org/10.1101/2020.02.21.959676; this version posted May 14, 2020. The copyright holder for this preprint (which was not certified by peer review) is the author/funder, who has granted bioRxiv a license to display the preprint in perpetuity. It is made available under aCC-BY-NC-ND 4.0 International license.

904 **References**

905 Amatniek JC, Hauser WA, DelCastillo-Castaneda C, Jacobs DM, Marder K, Bell K, Albert M, Brandt J,
906 Stern Y (2006) Incidence and predictors of seizures in patients with Alzheimer's disease.
907 Epilepsia 47:867–872.
908 Baimbridge KG, Miller JJ (1982) Immunohistochemical localization of calcium-binding protein in the
909 cerebellum, hippocampal formation and olfactory bulb of the rat. Brain Research 245:223–229.
910 Balmer TS (2016) Perineuronal Nets Enhance the Excitability of Fast-Spiking Neurons. eNeuro 3.
911 Barnes CA (1979) Memory deficits associated with senescence: a neurophysiological and behavioral
912 study in the rat. J Comp Physiol Psychol 93:74–104.
913 Baude A, Bleasdale C, Dalezios Y, Somogyi P, Klausberger T (2007) Immunoreactivity for the GABAA
914 receptor alpha1 subunit, somatostatin and Connexin36 distinguishes axoaxonic, basket, and
915 bistratified interneurons of the rat hippocampus. Cereb Cortex 17:2094–2107.
916 Berens P (2009) CircStat: A MATLAB Toolbox for Circular Statistics. Journal of Statistical Software 31:1–
917 21.
918 Born HA, Kim J-Y, Savjani RR, Das P, Dabaghian YA, Guo Q, Yoo JW, Schuler DR, Cirrito JR, Zheng
919 H, Golde TE, Noebels JL, Jankowsky JL (2014) Genetic suppression of transgenic APP rescues
920 Hypersynchronous network activity in a mouse model of Alzeimer's disease. J Neurosci 34:3826–
921 3840.
922 Braak H, Braak E (1991) Neuropathological stageing of Alzheimer-related changes. Acta Neuropathol
923 82:239–259.
924 Busche MA, Chen X, Henning HA, Reichwald J, Staufenbiel M, Sakmann B, Konnerth A (2012) Critical
925 role of soluble amyloid-β for early hippocampal hyperactivity in a mouse model of Alzheimer's
926 disease. PNAS 109:8740–8745.
927 Busche MA, Eichhoff G, Adelsberger H, Abramowski D, Wiederhold K-H, Haass C, Staufenbiel M,
928 Konnerth A, Garaschuk O (2008) Clusters of hyperactive neurons near amyloid plaques in a
929 mouse model of Alzheimer's disease. Science 321:1686–1689.
930 Buzsáki G (1986) Hippocampal sharp waves: their origin and significance. Brain Res 398:242–252.

bioRxiv preprint doi: https://doi.org/10.1101/2020.02.21.959676; this version posted May 14, 2020. The copyright holder for this preprint (which was not certified by peer review) is the author/funder, who has granted bioRxiv a license to display the preprint in perpetuity. It is made available under aCC-BY-NC-ND 4.0 International license.

931 Buzsáki G (2015) Hippocampal sharp wave-ripple: A cognitive biomarker for episodic memory and
932 planning. Hippocampus 25:1073–1188.
933 Buzsáki G, Leung LW, Vanderwolf CH (1983) Cellular bases of hippocampal EEG in the behaving rat.
934 Brain Res 287:139–171.
935 Buzsáki G, Logothetis N, Singer W (2013) Scaling brain size, keeping timing: evolutionary preservation
936 of brain rhythms. Neuron 80:751–764.
937 Carr MF, Karlsson MP, Frank LM (2012) Transient slow gamma synchrony underlies hippocampal
938 memory replay. Neuron 75:700–713.
939 Cattaud V, Bezzina C, Rey CC, Lejards C, Dahan L, Verret L (2018) Early disruption of parvalbumin
940 expression and perineuronal nets in the hippocampus of the Tg2576 mouse model of Alzheimer's
941 disease can be rescued by enriched environment. Neurobiol Aging 72:147–158.
942 Chen L, Saito T, Saido TC, Mody I (2018) Novel Quantitative Analyses of Spontaneous Synaptic Events
943 in Cortical Pyramidal Cells Reveal Subtle Parvalbumin-Expressing Interneuron Dysfunction in a
944 Knock-In Mouse Model of Alzheimer's Disease. eNeuro 5.
945 Ciupek SM, Cheng J, Ali YO, Lu H-C, Ji D (2015) Progressive Functional Impairments of Hippocampal
946 Neurons in a Tauopathy Mouse Model. J Neurosci 35:8118–8131.
947 Clements JD, Bekkers JM (1997) Detection of spontaneous synaptic events with an optimally scaled
948 template. Biophys J 73:220–229.
949 Cleveland WS (1979) Robust Locally Weighted Regression and Smoothing Scatterplots. Journal of the
950 American Statistical Association 74:829–836.
951 Colgin LL (2016) Rhythms of the hippocampal network. Nat Rev Neurosci 17:239–249.
952 Cowen SL, Gray DT, Wiegand J-PL, Schimanski LA, Barnes CA (2018) Age-associated changes in
953 waking hippocampal sharp-wave ripples. Hippocampus.
954 Csicsvari J, Hirase H, Czurkó A, Mamiya A, Buzsáki G (1999) Oscillatory Coupling of Hippocampal
955 Pyramidal Cells and Interneurons in the Behaving Rat. J Neurosci 19:274–287.
956 Dana H, Chen T-W, Hu A, Shields BC, Guo C, Looger LL, Kim DS, Svoboda K (2014) Thy1-GCaMP6
957 transgenic mice for neuronal population imaging in vivo. PLoS ONE 9:e108697.

bioRxiv preprint doi: https://doi.org/10.1101/2020.02.21.959676; this version posted May 14, 2020. The copyright holder for this preprint (which was not certified by peer review) is the author/funder, who has granted bioRxiv a license to display the preprint in perpetuity. It is made available under aCC-BY-NC-ND 4.0 International license.

958 Dickerson BC, Salat DH, Greve DN, Chua EF, Rand-Giovannetti E, Rentz DM, Bertram L, Mullin K, Tanzi
959 RE, Blacker D, Albert MS, Sperling RA (2005) Increased hippocampal activation in mild cognitive
960 impairment compared to normal aging and AD. Neurology 65:404–411.
961 Ego-Stengel V, Wilson MA (2010) Disruption of ripple-associated hippocampal activity during rest impairs
962 spatial learning in the rat. Hippocampus 20:1–10.
963 Ellender TJ, Nissen W, Colgin LL, Mann EO, Paulsen O (2010) Priming of Hippocampal Population Bursts
964 by Individual Perisomatic-Targeting Interneurons. J Neurosci 30:5979–5991.
965 Favuzzi E, Marques-Smith A, Deogracias R, Winterflood CM, Sánchez-Aguilera A, Mantoan L, Maeso P,
966 Fernandes C, Ewers H, Rico B (2017) Activity-Dependent Gating of Parvalbumin Interneuron
967 Function by the Perineuronal Net Protein Brevican. Neuron 95:639-655.e10.
968 Fernández-Ruiz A, Oliva A, Oliveira EF de, Rocha-Almeida F, Tingley D, Buzsáki G (2019) Long-duration
969 hippocampal sharp wave ripples improve memory. Science 364:1082–1086.
970 Foffani G, Uzcategui YG, Gal B, Menendez de la Prida L (2007) Reduced Spike-Timing Reliability
971 Correlates with the Emergence of Fast Ripples in the Rat Epileptic Hippocampus. Neuron 55:930–
972 941.
973 Gillespie AK, Jones EA, Lin Y-H, Karlsson MP, Kay K, Yoon SY, Tong LM, Nova P, Carr JS, Frank LM,
974 Huang Y (2016) Apolipoprotein E4 Causes Age-Dependent Disruption of Slow Gamma
975 Oscillations during Hippocampal Sharp-Wave Ripples. Neuron 90:740–751.
976 Girardeau G, Benchenane K, Wiener SI, Buzsáki G, Zugaro MB (2009) Selective suppression of
977 hippocampal ripples impairs spatial memory. Nat Neurosci 12:1222–1223.
978 Hájos N, Ellender TJ, Zemankovics R, Mann EO, Exley R, Cragg SJ, Freund TF, Paulsen O (2009)
979 Maintaining network activity in submerged hippocampal slices: importance of oxygen supply. Eur
980 J Neurosci 29:319–327.
981 Hauser WA, Morris ML, Heston LL, Anderson VE (1986) Seizures and myoclonus in patients with
982 Alzheimer's disease. Neurology 36:1226–1230.
983 Hazra A, Gu F, Aulakh A, Berridge C, Eriksen JL, Ziburkus J (2013) Inhibitory neuron and hippocampal
984 circuit dysfunction in an aged mouse model of Alzheimer's disease. PLoS ONE 8:e64318.

bioRxiv preprint doi: https://doi.org/10.1101/2020.02.21.959676; this version posted May 14, 2020. The copyright holder for this preprint (which was not certified by peer review) is the author/funder, who has granted bioRxiv a license to display the preprint in perpetuity. It is made available under aCC-BY-NC-ND 4.0 International license.

985 He M, Tucciarone J, Lee S, Nigro MJ, Kim Y, Levine JM, Kelly SM, Krugikov I, Wu P, Chen Y, Gong L,
986 Hou Y, Osten P, Rudy B, Huang ZJ (2016) Strategies and Tools for Combinatorial Targeting of
987 GABAergic Neurons in Mouse Cerebral Cortex. Neuron 91:1228–1243.
988 Hijazi S, Heistek TS, Scheltens P, Neumann U, Shimshek DR, Mansvelder HD, Smit AB, Kesteren RE
989 van (2019) Early restoration of parvalbumin interneuron activity prevents memory loss and
990 network hyperexcitability in a mouse model of Alzheimer's disease. Mol Psychiatry:1–19.
991 Hippenmeyer S, Vrieseling E, Sigrist M, Portmann T, Laengle C, Ladle DR, Arber S (2005) A
992 developmental switch in the response of DRG neurons to ETS transcription factor signaling. PLoS
993 Biol 3:e159.
994 Hollnagel J-O, Elzoheiry S, Gorgas K, Kins S, Beretta CA, Kirsch J, Kuhse J, Kann O, Kiss E (2019) Early
995 alterations in hippocampal perisomatic GABAergic synapses and network oscillations in a mouse
996 model of Alzheimer's disease amyloidosis. PLOS ONE 14:e0209228.
997 Iaccarino HF, Singer AC, Martorell AJ, Rudenko A, Gao F, Gillingham TZ, Mathys H, Seo J, Kritskiy O,
998 Abdurrob F, Adaikkan C, Canter RG, Rueda R, Brown EN, Boyden ES, Tsai L-H (2016) Gamma
999 frequency entrainment attenuates amyloid load and modifies microglia. Nature 540:230–235.
1000 Jones EA, Gillespie AK, Yoon SY, Frank LM, Huang Y (2019) Early Hippocampal Sharp-Wave Ripple
1001 Deficits Predict Later Learning and Memory Impairments in an Alzheimer's Disease Mouse Model.
1002 Cell Rep 29:2123-2133.e4.
1003 Jura B, Macrez N, Meyrand P, Bem T (2019) Deficit in hippocampal ripples does not preclude spatial
1004 memory formation in APP/PS1 mice. Sci Rep 9:1–12.
1005 Kamenetz F, Tomita T, Hsieh H, Seabrook G, Borchelt D, Iwatsubo T, Sisodia S, Malinow R (2003) APP
1006 processing and synaptic function. Neuron 37:925–937.
1007 Karlsson MP, Frank LM (2009) Awake replay of remote experiences in the hippocampus. Nat Neurosci
1008 12:913–918.
1009 Katona L, Lapray D, Viney TJ, Oulhaj A, Borhegyi Z, Micklem BR, Klausberger T, Somogyi P (2014)
1010 Sleep and Movement Differentiates Actions of Two Types of Somatostatin-Expressing GABAergic
1011 Interneuron in Rat Hippocampus. Neuron 82:872–886.

bioRxiv preprint doi: https://doi.org/10.1101/2020.02.21.959676; this version posted May 14, 2020. The copyright holder for this preprint (which was not certified by peer review) is the author/funder, who has granted bioRxiv a license to display the preprint in perpetuity. It is made available under aCC-BY-NC-ND 4.0 International license.

1012 Klausberger T, Somogyi P (2008) Neuronal Diversity and Temporal Dynamics: The Unity of Hippocampal
1013 Circuit Operations. Science 321:53–57.
1014 Kudrimoti HS, Barnes CA, McNaughton BL (1999) Reactivation of hippocampal cell assemblies: effects
1015 of behavioral state, experience, and EEG dynamics. J Neurosci 19:4090–4101.
1016 Kwok JCF, Dick G, Wang D, Fawcett JW (2011) Extracellular matrix and perineuronal nets in CNS repair.
1017 Dev Neurobiol 71:1073–1089.
1018 Lapray D, Lasztoczi B, Lagler M, Viney TJ, Katona L, Valenti O, Hartwich K, Borhegyi Z, Somogyi P,
1019 Klausberger T (2012) Behavior-dependent specialization of identified hippocampal interneurons.
1020 Nature Neuroscience 15:1265–1271.
1021 Le Van Quyen M, Bragin A, Staba R, Crépon B, Wilson CL, Engel J (2008) Cell type-specific firing during
1022 ripple oscillations in the hippocampal formation of humans. J Neurosci 28:6104–6110.
1023 Lee AK, Wilson MA (2002) Memory of sequential experience in the hippocampus during slow wave sleep.
1024 Neuron 36:1183–1194.
1025 Lee S-H, Marchionni I, Bezaire M, Varga C, Danielson N, Lovett-Barron M, Losonczy A, Soltesz I (2014)
1026 Parvalbumin-Positive Basket Cells Differentiate Among Hippocampal Pyramidal Cells. Neuron
1027 82:1129–1144.
1028 Lein ES et al. (2007) Genome-wide atlas of gene expression in the adult mouse brain. Nature 445:168–
1029 176.
1030 Li Y, Sun H, Chen Z, Xu H, Bu G, Zheng H (2016) Implications of GABAergic Neurotransmission in
1031 Alzheimer's Disease. Front Aging Neurosci 8:31.
1032 Madisen L, Zwingman TA, Sunkin SM, Oh SW, Zariwala HA, Gu H, Ng LL, Palmiter RD, Hawrylycz MJ,
1033 Jones AR, Lein ES, Zeng H (2010) A robust and high-throughput Cre reporting and
1034 characterization system for the whole mouse brain. Nat Neurosci 13:133–140.
1035 Mahar I, Albuquerque MS, Mondragon-Rodriguez S, Cavanagh C, Davoli MA, Chabot J-G, Williams S,
1036 Mechawar N, Quirion R, Krantic S (2016) Phenotypic Alterations in Hippocampal NPY- and PV-
1037 Expressing Interneurons in a Presymptomatic Transgenic Mouse Model of Alzheimer's Disease.
1038 Front Aging Neurosci 8:327.

bioRxiv preprint doi: https://doi.org/10.1101/2020.02.21.959676; this version posted May 14, 2020. The copyright holder for this preprint (which was not certified by peer review) is the author/funder, who has granted bioRxiv a license to display the preprint in perpetuity. It is made available under aCC-BY-NC-ND 4.0 International license.

1039 Maroteaux M, Liu SJ (2016) Alteration of AMPA Receptor-Mediated Synaptic Transmission by Alexa
1040 Fluor 488 and 594 in Cerebellar Stellate Cells. eNeuro 3 Available at:
1041 https://www.ncbi.nlm.nih.gov/pmc/articles/PMC4895128/ [Accessed July 26, 2018].
1042 Mattson MP (2004) Pathways towards and away from Alzheimer's disease. Nature 430:631–639.
1043 Miyawaki T, Norimoto H, Ishikawa T, Watanabe Y, Matsuki N, Ikegaya Y (2014) Dopamine receptor
1044 activation reorganizes neuronal ensembles during hippocampal sharp waves in vitro. PLoS ONE
1045 9:e104438.
1046 Mizuseki K, Buzsáki G (2013) Preconfigured, skewed distribution of firing rates in the hippocampus and
1047 entorhinal cortex. Cell Rep 4:1010–1021.
1048 Mizuseki K, Diba K, Pastalkova E, Buzsáki G (2011) Hippocampal CA1 pyramidal cells form functionally
1049 distinct sublayers. Nat Neurosci 14:1174–1181.
1050 Nádasdy Z, Hirase H, Czurkó A, Csicsvari J, Buzsáki G (1999) Replay and Time Compression of
1051 Recurring Spike Sequences in the Hippocampus. J Neurosci 19:9497–9507.
1052 Nicole O, Hadzibegovic S, Gajda J, Bontempi B, Bem T, Meyrand P (2016) Soluble amyloid beta
1053 oligomers block the learning-induced increase in hippocampal sharp wave-ripple rate and impair
1054 spatial memory formation. Sci Rep 6:22728.
1055 Norimoto H, Makino K, Gao M, Shikano Y, Okamoto K, Ishikawa T, Sasaki T, Hioki H, Fujisawa S,
1056 Ikegaya Y (2018) Hippocampal ripples down-regulate synapses. Science:eaao0702.
1057 Oakley H, Cole SL, Logan S, Maus E, Shao P, Craft J, Guillozet-Bongaarts A, Ohno M, Disterhoft J, Eldik
1058 LV, Berry R, Vassar R (2006) Intraneuronal β-Amyloid Aggregates, Neurodegeneration, and
1059 Neuron Loss in Transgenic Mice with Five Familial Alzheimer's Disease Mutations: Potential
1060 Factors in Amyloid Plaque Formation. J Neurosci 26:10129–10140.
1061 Ognjanovski N, Schaeffer S, Wu J, Mofakham S, Maruyama D, Zochowski M, Aton SJ (2017)
1062 Parvalbumin-expressing interneurons coordinate hippocampal network dynamics required for
1063 memory consolidation. Nat Commun 8:15039.
1064 Ohno M (2009) Failures to reconsolidate memory in a mouse model of Alzheimer's disease. Neurobiol
1065 Learn Mem 92:455–459.

bioRxiv preprint doi: https://doi.org/10.1101/2020.02.21.959676; this version posted May 14, 2020. The copyright holder for this preprint (which was not certified by peer review) is the author/funder, who has granted bioRxiv a license to display the preprint in perpetuity. It is made available under aCC-BY-NC-ND 4.0 International license.

1066 O'Neill J, Senior TJ, Allen K, Huxter JR, Csicsvari J (2008) Reactivation of experience-dependent cell
1067 assembly patterns in the hippocampus. Nat Neurosci 11:209–215.
1068 Palop JJ, Chin J, Roberson ED, Wang J, Thwin MT, Bien-Ly N, Yoo J, Ho KO, Yu G-Q, Kreitzer A,
1069 Finkbeiner S, Noebels JL, Mucke L (2007) Aberrant Excitatory Neuronal Activity and
1070 Compensatory Remodeling of Inhibitory Hippocampal Circuits in Mouse Models of Alzheimer's
1071 Disease. Neuron 55:697–711.
1072 Palop JJ, Mucke L (2009) Epilepsy and cognitive impairments in Alzheimer disease. Arch Neurol 66:435–
1073 440.
1074 Palop JJ, Mucke L (2010) Amyloid-beta-induced neuronal dysfunction in Alzheimer's disease: from
1075 synapses toward neural networks. Nat Neurosci 13:812–818.
1076 Pariente J, Cole S, Henson R, Clare L, Kennedy A, Rossor M, Cipoloti L, Puel M, Demonet JF, Chollet
1077 F, Frackowiak RSJ (2005) Alzheimer's patients engage an alternative network during a memory
1078 task. Ann Neurol 58:870–879.
1079 Pelkey KA, Barksdale E, Craig MT, Yuan X, Sukumaran M, Vargish GA, Mitchell RM, Wyeth MS, Petralia
1080 RS, Chittajallu R, Karlsson R-M, Cameron HA, Murata Y, Colonnese MT, Worley PF, McBain CJ
1081 (2015) Pentraxins coordinate excitatory synapse maturation and circuit integration of parvalbumin
1082 interneurons. Neuron 85:1257–1272.
1083 Pelkey KA, Chittajallu R, Craig MT, Tricoire L, Wester JC, McBain CJ (2017) Hippocampal GABAergic
1084 Inhibitory Interneurons. Physiol Rev 97:1619–1747.
1085 Pellow S, Chopin P, File SE, Briley M (1985) Validation of open:closed arm entries in an elevated plus-
1086 maze as a measure of anxiety in the rat. J Neurosci Methods 14:149–167.
1087 Pozueta J, Lefort R, Shelanski ML (2013) Synaptic changes in Alzheimer's disease and its models.
1088 Neuroscience 251:51–65.
1089 Roux L, Hu B, Eichler R, Stark E, Buzsáki G (2017) Sharp wave ripples during learning stabilize the
1090 hippocampal spatial map. Nat Neurosci.

bioRxiv preprint doi: https://doi.org/10.1101/2020.02.21.959676; this version posted May 14, 2020. The copyright holder for this preprint (which was not certified by peer review) is the author/funder, who has granted bioRxiv a license to display the preprint in perpetuity. It is made available under aCC-BY-NC-ND 4.0 International license.

1091 Sasaguri H, Nilsson P, Hashimoto S, Nagata K, Saito T, De Strooper B, Hardy J, Vassar R, Winblad B,
1092 Saido TC (2017) APP mouse models for Alzheimer's disease preclinical studies. The EMBO
1093 Journal 36:2473–2487.
1094 Schlingloff D, Káli S, Freund TF, Hájos N, Gulyás AI (2014) Mechanisms of sharp wave initiation and
1095 ripple generation. J Neurosci 34:11385–11398.
1096 Serrano-Pozo A, Frosch MP, Masliah E, Hyman BT (2011) Neuropathological Alterations in Alzheimer
1097 Disease. Cold Spring Harb Perspect Med 1:a006189.
1098 Shankar GM, Li S, Mehta TH, Garcia-Munoz A, Shepardson NE, Smith I, Brett FM, Farrell MA, Rowan
1099 MJ, Lemere CA, Regan CM, Walsh DM, Sabatini BL, Selkoe DJ (2008) Amyloid-beta protein
1100 dimers isolated directly from Alzheimer's brains impair synaptic plasticity and memory. Nat Med
1101 14:837–842.
1102 Skaggs WE, McNaughton BL (1996) Replay of neuronal firing sequences in rat hippocampus during
1103 sleep following spatial experience. Science 271:1870–1873.
1104 Slaker M, Churchill L, Todd RP, Blacktop JM, Zuloaga DG, Raber J, Darling RA, Brown TE, Sorg BA
1105 (2015) Removal of Perineuronal Nets in the Medial Prefrontal Cortex Impairs the Acquisition and
1106 Reconsolidation of a Cocaine-Induced Conditioned Place Preference Memory. J Neurosci
1107 35:4190–4202.
1108 Slomianka L, Amrein I, Knuesel I, Sørensen JC, Wolfer DP (2011) Hippocampal pyramidal cells: the
1109 reemergence of cortical lamination. Brain Struct Funct 216:301.
1110 Soltesz I, Losonczy A (2018) CA1 pyramidal cell diversity enabling parallel information processing in the
1111 hippocampus. Nat Neurosci 21:484–493.
1112 Somogyi P, Katona L, Klausberger T, Lasztóczi B, Viney TJ (2014) Temporal redistribution of inhibition
1113 over neuronal subcellular domains underlies state-dependent rhythmic change of excitability in
1114 the hippocampus. Phil Trans R Soc B 369:20120518.
1115 Sorg BA, Berretta S, Blacktop JM, Fawcett JW, Kitagawa H, Kwok JCF, Miquel M (2016) Casting a Wide
1116 Net: Role of Perineuronal Nets in Neural Plasticity. J Neurosci 36:11459–11468.

bioRxiv preprint doi: https://doi.org/10.1101/2020.02.21.959676; this version posted May 14, 2020. The copyright holder for this preprint (which was not certified by peer review) is the author/funder, who has granted bioRxiv a license to display the preprint in perpetuity. It is made available under aCC-BY-NC-ND 4.0 International license.

1117 Stoiljkovic M, Kelley C, Stutz B, Horvath TL, Hajós M (2018) Altered Cortical and Hippocampal Excitability
1118 in TgF344-AD Rats Modeling Alzheimer's Disease Pathology. Cereb Cortex.
1119 Sun ZY, Bozzelli PL, Caccavano A, Allen M, Balmuth J, Vicini S, Wu J-Y, Conant K (2017) Disruption of
1120 perineuronal nets increases the frequency of sharp wave ripple events. Hippocampus.
1121 Ting JT, Daigle TL, Chen Q, Feng G (2014) Acute brain slice methods for adult and aging animals:
1122 application of targeted patch clamp analysis and optogenetics. Methods Mol Biol 1183:221–242.
1123 Ting JT, Lee BR, Chong P, Soler-Llavina G, Cobbs C, Koch C, Zeng H, Lein E (2018) Preparation of
1124 Acute Brain Slices Using an Optimized N-Methyl-D-glucamine Protective Recovery Method. J Vis
1125 Exp.
1126 Toepper M (2017) Dissociating Normal Aging from Alzheimer's Disease: A View from Cognitive
1127 Neuroscience. Journal of Alzheimer's Disease 57:331–352.
1128 Tohda C, Urano T, Umezaki M, Nemere I, Kuboyama T (2012) Diosgenin is an exogenous activator of
1129 1,25D_3-MARRS/Pdia3/ERp57 and improves Alzheimer's disease pathologies in 5XFAD mice. Sci
1130 Rep 2:535.
1131 Valero M, Cid E, Averkin RG, Aguilar J, Sanchez-Aguilera A, Viney TJ, Gomez-Dominguez D, Bellistri E,
1132 de la Prida LM (2015) Determinants of different deep and superficial CA1 pyramidal cell dynamics
1133 during sharp-wave ripples. Nat Neurosci 18:1281–1290.
1134 Varga C, Golshani P, Soltesz I (2012) Frequency-invariant temporal ordering of interneuronal discharges
1135 during hippocampal oscillations in awake mice. Proc Natl Acad Sci USA 109:E2726-2734.
1136 Varga C, Oijala M, Lish J, Szabo GG, Bezaire M, Marchionni I, Golshani P, Soltesz I (2014) Functional
1137 fission of parvalbumin interneuron classes during fast network events. eLife 3:e04006.
1138 Ven GM van de, Trouche S, McNamara CG, Allen K, Dupret D (2016) Hippocampal Offline Reactivation
1139 Consolidates Recently Formed Cell Assembly Patterns during Sharp Wave-Ripples. Neuron
1140 92:968–974.
1141 Verret L, Mann EO, Hang GB, Barth AMI, Cobos I, Ho K, Devidze N, Masliah E, Kreitzer AC, Mody I,
1142 Mucke L, Palop JJ (2012) Inhibitory interneuron deficit links altered network activity and cognitive
1143 dysfunction in Alzheimer model. Cell 149:708–721.

bioRxiv preprint doi: https://doi.org/10.1101/2020.02.21.959676; this version posted May 14, 2020. The copyright holder for this preprint (which was not certified by peer review) is the author/funder, who has granted bioRxiv a license to display the preprint in perpetuity. It is made available under aCC-BY-NC-ND 4.0 International license.

1144 Viney TJ, Lasztoczi B, Katona L, Crump MG, Tukker JJ, Klausberger T, Somogyi P (2013) Network state-
1145 dependent inhibition of identified hippocampal CA3 axo-axonic cells *in vivo*. Nature Neuroscience
1146 16:1802–1811.

1147 Vossel KA, Beagle AJ, Rabinovici GD, Shu H, Lee SE, Naasan G, Hegde M, Cornes SB, Henry ML,
1148 Nelson AB, Seeley WW, Geschwind MD, Gorno-Tempini ML, Shih T, Kirsch HE, Garcia PA, Miller
1149 BL, Mucke L (2013) Seizures and epileptiform activity in the early stages of Alzheimer disease.
1150 JAMA Neurol 70:1158–1166.

1151 Wiegand J-PL, Gray DT, Schimanski LA, Lipa P, Barnes CA, Cowen SL (2016) Age Is Associated with
1152 Reduced Sharp-Wave Ripple Frequency and Altered Patterns of Neuronal Variability. J Neurosci
1153 36:5650–5660.

1154 Wilson MA, McNaughton BL (1994) Reactivation of hippocampal ensemble memories during sleep.
1155 Science 265:676–679.

1156 Wobbrock JO, Findlater L, Gergle D, Higgins JJ (2011) The Aligned Rank Transform for Nonparametric
1157 Factorial Analyses Using Only Anova Procedures. In: Proceedings of the SIGCHI Conference on
1158 Human Factors in Computing Systems, pp 143–146 CHI '11. New York, NY, USA: ACM. Available
1159 at: http://doi.acm.org/10.1145/1978942.1978963 [Accessed December 12, 2019].

1160 Xiao M-F et al. (2017) NPTX2 and cognitive dysfunction in Alzheimer's Disease. Elife 6.

1161 Yamada J, Jinno S (2015) Subclass-specific formation of perineuronal nets around parvalbumin-
1162 expressing GABAergic neurons in Ammon's horn of the mouse hippocampus. J Comp Neurol
1163 523:790–804.

1164 Yang X, Yao C, Tian T, Li X, Yan H, Wu J, Li H, Pei L, Liu D, Tian Q, Zhu L-Q, Lu Y (2016) A novel
1165 mechanism of memory loss in Alzheimer's disease mice via the degeneration of entorhinal-CA1
1166 synapses. Mol Psychiatry.

1167 Ylinen A, Bragin A, Nadasdy Z, Jando G, Szabo I, Sik A, Buzsaki G (1995) Sharp wave-associated high-
1168 frequency oscillation (200 Hz) in the intact hippocampus: network and intracellular mechanisms.
1169 J Neurosci 15:30–46.

bioRxiv preprint doi: https://doi.org/10.1101/2020.02.21.959676; this version posted May 14, 2020. The copyright holder for this preprint (which was not certified by peer review) is the author/funder, who has granted bioRxiv a license to display the preprint in perpetuity. It is made available under aCC-BY-NC-ND 4.0 International license.

1170 Youmans KL, Tai LM, Kanekiyo T, Stine WB, Michon S-C, Nwabuisi-Heath E, Manelli AM, Fu Y, Riordan
1171 S, Eimer WA, Binder L, Bu G, Yu C, Hartley DM, LaDu MJ (2012) Intraneuronal Aβ detection in
1172 5xFAD mice by a new Aβ-specific antibody. Mol Neurodegener 7:8.
1173 Zott B, Busche MA, Sperling RA, Konnerth A (2018) What Happens with the Circuit in Alzheimer's
1174 Disease in Mice and Humans? Annu Rev Neurosci 41:277–297.
1175

bioRxiv preprint doi: https://doi.org/10.1101/2020.02.21.959676; this version posted May 14, 2020. The copyright holder for this preprint (which was not certified by peer review) is the author/funder, who has granted bioRxiv a license to display the preprint in perpetuity. It is made available under aCC-BY-NC-ND 4.0 International license.

1176 **Legends**

1177 **Table 1: *Mouse cohorts used in study*.** *Top*, Electrophysiology/imaging cohorts were distinct from
1178 behavioral cohorts. For both experiments, mice were studied at an age of 1 and 3 months (mo). *Bottom*,
1179 The 3 mo electrophysiology/imaging cohort consisted of three sub-cohorts with different reporter genes.

bioRxiv preprint doi: https://doi.org/10.1101/2020.02.21.959676; this version posted May 14, 2020. The copyright holder for this preprint (which was not certified by peer review) is the author/funder, who has granted bioRxiv a license to display the preprint in perpetuity. It is made available under aCC-BY-NC-ND 4.0 International license.

1180 **Figure 1:** ***Three month (mo) 5xFAD mice deposit amyloid and display minor impairment in spatial***
1181 ***memory***. ***A,*** Representative IHC in the CA1 – subiculum region in 1 mo (*top*) and 3 mo (*bottom*) for
1182 control (CT, *left*) and 5xFAD (*right*) mice. Red: MOAB-2, labeling both intraneuronal and extracellular Aβ,
1183 including unaggregated, oligomeric, and fibrillar $A\beta_{42}$ and unaggregated $A\beta_{40}$. Cyan: Thioflavin-S, labeling
1184 fibrils in extracellular plaques. Staining was repeated in 2 mice of each genotype and age. Scale bar =
1185 100 µm. Inset scale bars = 50 µm. ***B,*** Cohorts of 1 mo (n_{mice} = 10 CT, 10 5xFAD, *top*) and 3 mo (n_{mice} =
1186 15 CT, 12 5xFAD, *bottom*) mice, were trained on the Barnes Maze, consisting of four days of training,
1187 each with four 180 s trials. The latency to find the target escape hole was averaged over the four trials.
1188 ***C,*** Latency to find target on the final 90 s probe trial on the fifth day for 1 mo (*top*) and 3 mo (*bottom*)
1189 cohorts. ***D***, Representative heat map for 3 mo animals on the final probe trial. Warmer colors represent
1190 longer duration. Control mice spent more time at the target and surrounding region than 5xFAD mice.
1191 For all plots, individual data points represent an animal. Closed circles represent males, open circles
1192 females. Box-whisker plots represent non-normal data as Median and IQRs. p-values indicated above
1193 brackets.

bioRxiv preprint doi: https://doi.org/10.1101/2020.02.21.959676; this version posted May 14, 2020. The copyright holder for this preprint (which was not certified by peer review) is the author/funder, who has granted bioRxiv a license to display the preprint in perpetuity. It is made available under aCC-BY-NC-ND 4.0 International license.

1194 **Figure 2**: ***Sharp wave ripples are increased in 3 month 5xFAD mice***. ***A***, SWRs were recorded in acute
1195 horizontal slices with the LFP electrode located in CA1. ***B***, Example traces of 3 mo control (*left*) and
1196 5xFAD (*right*) slices. *1st trace*, LFP filtered between 1-1000 Hz, raster below indicates detected SWR
1197 events as overlap of sharp wave (SW) and ripple events. *2nd trace*, SW, filtered between 1-30 Hz, raster
1198 below indicates detected SW events. *3rd trace*, low gamma, filtered between 20-50 Hz. *4th trace*, ripple,
1199 filtered between 120-220 Hz, raster below indicates detected ripple events. *Bottom*, z-scored time-
1200 frequency spectrogram from 1-250 Hz. ***C***, Summary plot of SWR event frequency for 5xFAD and
1201 littermate controls for both 1 mo (n_{mice} = 10 CT, 10 5xFAD; *left*) and 3 mo cohorts (n_{mice} = 27 CT, 29
1202 5xFAD; *right*). ***D***, SWR event amplitude and duration. ***E***, Peak ripple frequency and the number of ripple
1203 cycles within SWR duration. ***F***, Example SWR events for traces displayed in ***B***, with average z-scored
1204 time-frequency spectrogram of all events below. ***G***, Average Fast-Fourier Transform (FFT) of 200 ms
1205 window around all SWR events from characteristic subset of n_{slice} = 7 CT, 7 5xFAD from n_{mice} = 4 CT, 5
1206 5xFAD. Shaded region represents SEM. ***H-J***, SWR-locked oscillation power in the low gamma (20-50
1207 Hz, ***H***), ripple (120-220 Hz, ***I***), and fast ripple (250-500 Hz, ***J***) ranges. Note that in ***H***, one value was
1208 identified as an outlier by the ROUT method but was retained in analysis, as the data point appeared
1209 valid, and even with removal did not alter the observed increase (U = 193, p = 0.0015; Mann-Whitney).
1210 For all plots, individual data points represent the average of all slices recorded from an animal
1211 (n_{slice}/animal in Table 1). Closed circles represent males, open circles females. Bar plots indicate normal
1212 data with Mean ± SEM. Box-whisker plots represent non-normal data with Median and IQRs. p-values
1213 indicated above brackets.

bioRxiv preprint doi: https://doi.org/10.1101/2020.02.21.959676; this version posted May 14, 2020. The copyright holder for this preprint (which was not certified by peer review) is the author/funder, who has granted bioRxiv a license to display the preprint in perpetuity. It is made available under aCC-BY-NC-ND 4.0 International license.

1214 **Figure 3**: ***Altered ensembles of pyramidal cells are recruited in 5xFAD slices***. ***A***, Confocal imaging
1215 of PC ensembles were recorded concurrently with SWRs. Scale bars = 50 µm. ***B***, *Post hoc* IHC for
1216 Calbindin (CB) of imaged Thy1-GCaMP6f (GC) slices. Dashed grey lines approximately distinguish layers
1217 of hippocampus, *str. rad.* = *stratum radiatum*, *str. pyr.* = *stratum pyramidale, str. or.* = *stratum oriens*.
1218 Scale bar = 50 µm. ***C***, Histogram of the distance from the center of the cell body to the *str. pyr./rad.* border
1219 for 539 GC+ CB-, 292 GC- CB+, and 146 GC+ CB+ cells pooled from n_{slice} = 4 from n_{mice} = 2 CT, 2 5xFAD.
1220 ***D***, LFP and ΔF/F for identified cells in slices from 3 mo control (*left*) and 5xFAD (*right)* mice*. Top trace,*
1221 LFP trace with identified SWR events in raster below. *Middle traces*, individual ΔF/F for each cell,
1222 superficial PCs (sPC) in magenta, and deep PCs (dPCs) in green. *Bottom raster*, identified Ca^{2+} events
1223 above threshold. Dark colored event indicate concurrence with SWR, light gray indicates spontaneous
1224 event. ***E***, The total number of active sPCs and dPCs for CT (n_{slice} = 25) and 5xFAD (n_{slice} = 23) slices. ***F***,
1225 The number of sPCs/dPCs active during SWRs. ***G***, Frequency, ***H***, Amplitude, and ***I***, Duration of Ca^{2+}
1226 transient events averaged across sPCs and dPCs for each slice. ***J***, *top*, Event matrix displaying for one
1227 example recording, the SWR events on the x-axis, and cells on the y-axis (magenta = sPC, green = dPC).
1228 *Bottom left*, pairwise Jaccard similarity between SWR events (columns in event matrix). Similarity matrix
1229 is symmetric and the diagonal = 1 by definition - these have not been plotted for clarity. *Bottom right*,
1230 pairwise Jaccard similarity between cells (rows in event matrix). Dashed lines indicate borders between
1231 sPC-sPC, sPC-dPC, and dPC-dPC comparisons. Quantification of cell similarity was performed by
1232 grouping all sPC-PC comparisons (sPC-sPC & sPC-dPC), and all dPC-PC comparisons (dPC-dPC &
1233 sPC-dPC). Cumulative distribution functions were calculated from all pairwise comparisons for ***K***, SWR-
1234 SWR similarity, ***L***, sPC-PC similarity, and ***M***, dPC-PC similar. ***K-M*** all showed significant genotype
1235 differences via 2-way ANOVAs; asterisks indicate regions surviving multiple comparisons. * $p < 0.05$, **
1236 $p < 0.01$, *** $p < 0.001$. Box-whisker plots represent non-normal data with Median and IQRs. Individual
1237 data points represent a slice. Closed circles represent slices from males, open circles females. p-values
1238 of pairwise comparisons indicated above brackets.

bioRxiv preprint doi: https://doi.org/10.1101/2020.02.21.959676; this version posted May 14, 2020. The copyright holder for this preprint (which was not certified by peer review) is the author/funder, who has granted bioRxiv a license to display the preprint in perpetuity. It is made available under aCC-BY-NC-ND 4.0 International license.

1239 **Figure 4**: ***Pyramidal cell spiking is relatively unchanged in 5xFAD mice. A***, Diagram of a loose cell-
1240 attached recording of spikes from a Thy1-GCaMP6f+ pyramidal cell (PC) paired with LFP recording of
1241 SWRs. ***B***, Example traces from 3 mo control (*left*) and 5xFAD (*right*) slice. *Top trace*, LFP with SWR
1242 events in raster below. Gray shaded events indicate spontaneous SWR. Green shading indicates SWR
1243 coincident with at least one spike. Dark green shading indicates SWR coincident with burst, defined as 3
1244 or more spikes each within 60 ms. *Bottom trace*, Cell-attached recording from PC. Detected spikes and
1245 bursts indicated in raster below. Dark shading indicates they are coincident with SWR event, light gray
1246 shading indicates spontaneous events. Spike rates were calculated separately during spontaneous and
1247 SWR periods for ***C***, superficial PCs (sPC), n_{sPC} = 13 CT, 9 5xFAD, and ***D***, deep PCs (dPCs), n_{dPC} = 26
1248 CT, 35 5xFAD. The peri-SWR spike probability was calculated for ***E***, sPCs and ***F***, dPCs, by binning
1249 spikes into 100 2 ms bins and normalizing by total number of SWRs. Dark lines indicate average of all
1250 cells within a genotype, shaded regions indicate SEM. 0 ms indicates time of SWR peak. ***G***, The rate of
1251 bursts for sPCs and dPCs, defined as at least 3 spikes each within 60 ms. ***H***, Intra-burst interval for sPCs
1252 and dPCs, defined as the average time between successive spikes in a burst. ***I***, The fraction of spikes
1253 that occurred during SWRs. ***J***, The fraction of SWRs that had one or more spikes. ***K***, Example of SWR
1254 (*top trace*), with filtered slow gamma (20-50 Hz) and ripple (120-220 Hz) signals (*middle traces*). The
1255 phase of oscillations was set at 0° at peaks and 180° at troughs. *Bottom trace*, cell-attached recording,
1256 with spike times marked by vertical dashed lines. ***L-O***, Polar phase plots of phase-locking of spikes to
1257 SWR-nested slow gamma (***L-M***) and ripple (***N-O***) for sPCs (***L,N***) and dPCs (***M,O***). The angles of
1258 individual data points represent the average phase of all spikes for a cell. Length from origin (0-1)
1259 indicates the degree of phase-locking. A length of 1 signifies perfect phase-locking (every spike at same
1260 phase); a length of 0 indicates random or no phase-locking. Lines with arrowheads represent cell
1261 average, solid colored = CT, dashed grey = 5xFAD. Asterisks indicate result of Raleigh's test for non-
1262 uniformity, * $p < 0.05$, ** $p < 0.01$. p values indicate results of circular mean comparison. For all plots,
1263 individual data points represent a cell. Closed circles represent cells from males, open circles females.
1264 Box-whisker plots represent non-normal data as Median and IQRs. p-values of pairwise comparisons
1265 indicated above brackets.

bioRxiv preprint doi: https://doi.org/10.1101/2020.02.21.959676; this version posted May 14, 2020. The copyright holder for this preprint (which was not certified by peer review) is the author/funder, who has granted bioRxiv a license to display the preprint in perpetuity. It is made available under aCC-BY-NC-ND 4.0 International license.

1266 **Figure 5**: ***Pyramidal cells receive increased synaptic E/I ratio***. ***A***, Example traces of LFP + whole-cell
1267 recording voltage-clamped at -70 mV in Thy1-GCaMP6f littermate controls and 5xFAD/+;Thy1-GCaMP6f
1268 mice. Excitatory post-synaptic potentials (EPSCs) were sorted as spontaneous (sEPSCs) or SWR-
1269 coincident (swrEPSCs). ***B***, Example swrEPSCs. ***C***, Example traces of LFP + whole-cell recording
1270 voltage-clamped at 0 mV to detect sIPSCs and swrIPSCs. ***D***, Example swrIPSCs. ***E-H***, Summary plots
1271 of sEPSC frequency (***E***), amplitude (***F***), rise tau (***G***), and decay tau (***H***) for sPCs and dPCs in control and
1272 5xFAD mice (n_{sPC} = 7 CT, 5 5xFAD; n_{dPC} = 12 CT, 9 5xFAD). ***I***, sEPSQ = normalized spontaneous
1273 excitatory charge (integrated current per unit time). ***J***, swrEPSQ = total excitatory charge during SWRs,
1274 integrated over a 100 ms window centered around the SWR peak. ***K-N***, Summary plots of sIPSC
1275 frequency (***K***), amplitude (***L***), rise tau (***M***), and decay tau (***N***) (n_{sPC} = 7 CT, 5 5xFAD; n_{dPC} = 14 CT, 11
1276 5xFAD). ***O-P,*** Cumulative distribution functions, averaged over all cells for sIPSC amplitude (***O***) and
1277 decay tau (***P***), both for sPCs (*top*) and dPCs (*bottom*). Dark lines represent cell average, shaded region
1278 represents SEM. ***Q***, sIPSQ = normalized spontaneous inhibitory charge (integrated current per unit time).
1279 ***R***, swrIPSQ = total inhibitory charge during SWRs. ***S***, Spontaneous synaptic E/I ratio of normalized
1280 charge for each cell (sEPSQ/sIPSQ). ***T***, Synaptic E/I ratio for 100 ms window centered around SWR peak
1281 (swrEPSQ/swrIPSQ). ***U-V***, During SWRs, the charge for each cell (EPSQ and IPSQ) was calculated in
1282 2 ms bins by integrating the current in a sliding 100 ms window centered around that bin, for both sPCs
1283 (***U***) and dPCs (***V***). Summary data in ***J*** and ***R*** thus represent these curves at the y-intercept. Asterisks
1284 indicate regions that survived Šidák's multiple comparisons * < 0.05, ** < 0.01, *** < 0.01. ***W-X,*** the ratios
1285 of curves in ***U-V*** yield the synaptic E/I ratio during SWRs. Summary data in ***T*** represents these curves at
1286 the y-intercept. For all plots, individual data points represent a cell. Closed circles represent cells from
1287 males, open circles females. Box-whisker plots represent non-normal data with Median and IQRs. Bar
1288 plots represent normal data with Mean ± SEM. p-values of pairwise comparisons indicated above
1289 brackets.

bioRxiv preprint doi: https://doi.org/10.1101/2020.02.21.959676; this version posted May 14, 2020. The copyright holder for this preprint (which was not certified by peer review) is the author/funder, who has granted bioRxiv a license to display the preprint in perpetuity. It is made available under aCC-BY-NC-ND 4.0 International license.

1290 **Figure 6**: ***PV cells in CA1 delineate into basket (PVBCs), bistratified (PVBSCs), and axo-axonic***
1291 ***(PVAACs) cells. A***, Diagram of LFP + PV cell recording in 3 mo 5xFAD/+; PV^{Cre}/+;tdTom/+ and
1292 PV^{Cre}/+;tdTom/+ littermate controls. ***B***, Diagram of PV cell subtypes and their axonal targets in CA1 *str.*
1293 *pyr.* Examples of ***C.1***, PVBCs, ***C.2***, PVBSCs, and ***C.3***, PVAACs. Green fluorescence indicates avidin-
1294 fluorescein bound to the biocyin in the filled PV cell. Red fluorescence indicates PV^{Cre}/+;tdTom/+
1295 expression. Dashed grey lines approximately distinguish layers of hippocampus, *str. l.m.* = *stratum*
1296 *lacunosum-moleculare*, *str. rad.* = *stratum radiatum*, *str. pyr.* = *stratum pyramidale, str. or.* = *stratum*
1297 *oriens*. Notice that *str. pyr.* is dimly red due to the expression of other non-filled PVBCs targeting
1298 perisomatic regions of PCs. Scale bars = 100 µm. *Bottom traces*, Examples of LFP and cell-attached
1299 recording of spikes, which was used to aid in distinguishing PVBCs and PVAACs. PVAACs are unique
1300 in that they reduce their firing during SWRs. ***C.4***, Ankyrin G immunostaining showing co-localization of
1301 synaptic boutons with AIS of PCs for identified PVAAC. Scale bar = 10 µm. ***D***, Proportions of sorted cells
1302 in each genotype.

bioRxiv preprint doi: https://doi.org/10.1101/2020.02.21.959676; this version posted May 14, 2020. The copyright holder for this preprint (which was not certified by peer review) is the author/funder, who has granted bioRxiv a license to display the preprint in perpetuity. It is made available under aCC-BY-NC-ND 4.0 International license.

1303 **Figure 7**: ***PV basket cells have selectively reduced spiking***. Spiking data for PVBCs (panel sub-
1304 heading ***1***), PVBSCs (panel sub-heading ***2***), and PVAACs (panel sub-heading ***3***). ***A***, Example LFP and
1305 cell-attached traces for CT (*left*) and 5xFAD (*right*), for a PVBC (***A.1***), PVBSC (***A.2***), and PVAAC (***A.3***).
1306 Spike and SWR events are color-coded as in Fig. 4B. ***B***, Summary spike rate data for PVBCs (n_{PVBC} =
1307 13 CT, 16 5xFAD, ***B.1***), PVBSCs (n_{PVBSC} = 5 CT, 10 5xFAD, ***B.2***), and PVAACs (n_{PVAAC} = 6 CT, 6 5xFAD,
1308 ***B.3***) during spontaneous and SWR periods. ***C***, Peri-SWR spike probability. Asterisks indicate regions
1309 surviving Šidák's multiple comparisons correction. ***D***, Burst rate, defined as 3 or more spikes each within
1310 40 ms. ***E***, The fraction of SWRs with one or more spike. ***F***, The fraction of SWRs with a burst. ***G-H***, Polar
1311 phase plots of phase-locking of spikes to SWR-nested slow gamma (***G***) and ripple (***H***). The angles of
1312 individual data points represent the average phase of all spikes for a cell. Length from origin (0-1)
1313 indicates the degree of phase-locking. Lines with arrowheads represent cell average, solid colored = CT,
1314 dashed grey = 5xFAD. Asterisks indicate result of Raleigh's test for non-uniformity, p values indicate
1315 results of Watson-Williams or circular mean test. * < 0.05, ** < 0.01, *** < 0.001. For all plots, individual
1316 data points represent a cell. Closed circles represent cells from males, open circles females. Box-whisker
1317 plots represent non-normal data with Median and IQRs. p-values indicated above brackets.

bioRxiv preprint doi: https://doi.org/10.1101/2020.02.21.959676; this version posted May 14, 2020. The copyright holder for this preprint (which was not certified by peer review) is the author/funder, who has granted bioRxiv a license to display the preprint in perpetuity. It is made available under aCC-BY-NC-ND 4.0 International license.

1318 **Figure 8**: ***PV basket cells have selective decrease in excitatory synaptic input and decreased E/I***
1319 ***ratio***. Whole-cell data for PVBC EPSCs (panel sub-heading ***1***), PVBSC EPSCs (panel sub-heading ***2***),
1320 PVAAC EPSCs (panel sub-heading ***3***), and PVBC IPSCs (panel sub-heading ***4***). ***A***, Example recordings
1321 of LFP + whole-cell PV cell recording in 3 mo 5xFAD/+; PV^{Cre}/+;tdTom/+ and PV^{Cre}/+;tdTom/+ littermate
1322 controls, recording synaptic input during spontaneous and SWR period. EPSCs were recorded at -70 mV
1323 in PVBCs (***A.1***), PVBSCs (***A.2***), and PVAACs (***A.3***), and IPSCs recorded at 0 mV in a subset of PVBCs
1324 (***A.4***). ***B***, Summary data for spontaneous PSC frequency and amplitude for PVBC sEPSCs (n_{PVBC} = 12
1325 CT, 16 5xFAD, ***B.1***), PVBSC sEPSCs (n_{PVBSC} = 4 CT, 6 5xFAD, ***B.2***), PVAAC sEPSCs (n_{PVAAC} = 5 CT, 6
1326 5xFAD, ***B.3***), and PVBC sIPSCs (n_{PVBC} = 8 CT, 8 5xFAD, ***B.4***). ***C***, Spontaneous PSC kinetics: rise and
1327 decay tau. ***D***, Cumulative distribution function of PVBC decay tau. Dark lines represent cell average,
1328 shaded region represents SEM. ***E***, swrEPSQ and swrIPSQ = total excitatory and inhibitory charge during
1329 SWRs, integrated over a 100 ms window centered around the SWR peak. ***F***, *left*, PVBC spontaneous
1330 synaptic E/I ratio of normalized charge (sEPSQ/sIPSQ). ***F***, *right*, PVBC synaptic E/I ratio for 100 ms
1331 window centered around SWR peak (swrEPSQ/swrIPSQ). ***G***, The charge for each PVBC (EPSQ and
1332 IPSQ), calculated in 2 ms bins by integrating the current in a sliding 100 ms window centered around that
1333 bin. Summary data in ***E.1*** and ***E.4*** thus represent these curves at the y-intercept. Asterisks indicate
1334 regions that survived Šidák's multiple comparisons * < 0.05, ** < 0.01, *** < 0.01. ***H,*** the ratios of curves
1335 in ***G*** yield the synaptic E/I ratio during SWRs. Summary data in ***F*** represents these curves at the y-
1336 intercept. ***I***, Linear regression of spike rate during SWRs vs the E/I ratio. For all plots, individual data
1337 points represent a cell. Closed circles represent cells from males, open circles females. Bar plots
1338 represent normal data with Mean ± SEM. p-values indicated above brackets.

bioRxiv preprint doi: https://doi.org/10.1101/2020.02.21.959676; this version posted May 14, 2020. The copyright holder for this preprint (which was not certified by peer review) is the author/funder, who has granted bioRxiv a license to display the preprint in perpetuity. It is made available under aCC-BY-NC-ND 4.0 International license.

1339 **Figure 9**: ***Schematic of alterations to the CA1 micro-circuit in 5xFAD mice***. In PVBCs, the synaptic
1340 E/I ratio during SWRs was reduced, with a reduction in spike rate during SWRs. In sPCs, there was a
1341 reduction in sIPSCs, an increased E/I ratio during SWRs, and an increased probability of spiking during
1342 SWRs. In dPCs, there was an increase in synaptic E/I during spontaneous periods (between SWRs), no
1343 change in the E/I ratio during SWRs (with concomitant increases in excitation and inhibition), and
1344 enlarged ensembles.

	Electrophysiology + Imaging (Fig. 2-8)				Behavior (Fig. 1)			
	Control 1mo	*5xFAD 1mo*	***Control 3mo***	***5xFAD 3mo***	*Control 1mo*	*5xFAD 1mo*	*Control 3mo*	*5xFAD 3mo*
n_{mice}	10 (6f)	10 (4f)	27 (17f)	29 (12f)	10 (2f)	10 (6f)	15 (7f)	12 (8f)
Age (postnatal days)	40.2 ± 4.4	40.4 ± 4.6	95.8 ± 6.0	94.5 ± 5.8	42.0 ± 5.2	43.8 ± 4.2	91.8 ± 5.2	92.5 ± 5.4
n_{slice} *(range 2 - 8)*	5.6 ± 0.8	4.0 ± 1.8	3.9 ± 1.3	3.2 ± 1.4				
% slices with SWRs	93.8 ± 8.1%	70.8 ± 22.0%	72.4 ± 19.8%	66.3 ± 26.1%				

	Thy1-GCaMP6f (Fig. 3-5)		PV^{Cre}-tdTom (Fig. 6-8)		Thy1-GCaMP6f;PV^{Cre}-tdTom (Fig. 4-8)	
	Control	*5xFAD*	*Control*	*5xFAD*	*Control*	*5xFAD*
n_{mice}	10 (5f)	11 (5f)	13 (8f)	11 (5f)	4 (4f)	7 (2f)
Age (postnatal days)	95.0 ± 7.4	93.4 ± 3.2	96.8 ± 5.7	97.4 ± 6.0	94.8 ± 3.2	91.6 ± 2.1
n_{slice} *(range 2 - 8)*	3.9 ± 1.1	2.8 ± 1.3	3.8 ± 1.5	4.9 ± 2.1	4.5 ± 1.3	3.6 ± 1.8
% slices with SWRs	75.5 ± 20.2%	67.9 ± 26.2%	67.4 ± 20.5%	68.2 ± 25.3%	80.8 ± 16.4%	60.7 ± 30.5%
$n_{cell\text{-}attached}$	39 (PC)	39 (PC)	13 (PV)	18 (PV)	11 (PV)	5 (PC); 14 (PV)
$n_{whole\text{-}cell}$	21 (PC)	15 (PC)	11 (PV)	16 (PV)	10 (PV)	1 (PC); 13 (PV)

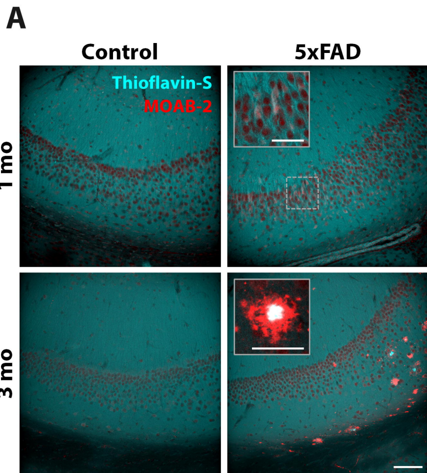
A
Control
5xFAD
Thioflavin-S
MOAB-2
1 mo
3 mo

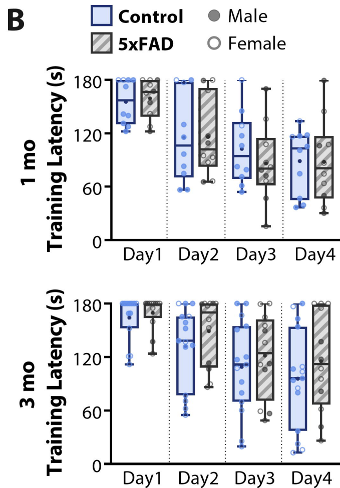
B
Control
5xFAD
Male
Female
1 mo
Training Latency (s)
180
120
60
0
Day1
Day2
Day3
Day4
3 mo
Training Latency (s)

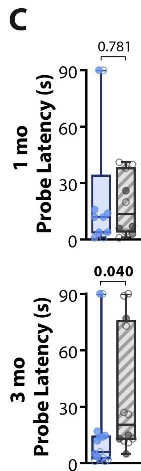
C
0.781
1 mo
Probe Latency (s)
90
60
30
0
0.040
3 mo
Probe Latency (s)

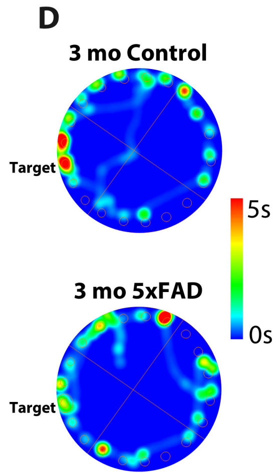
D
3 mo Control
Target
3 mo 5xFAD
Target
5s
0s

A
LFP
str. oriens
CA1
CA2
str. pyramidale
str. radiatum
str. lac. mol.
str. lucidum
CA3
DG
B
Control (3mo)
5xFAD (3mo)
1s
100μV
LFP (1-1000Hz)
Sharp Wave (1-30Hz)
Low Gamma (20-50Hz)
Ripple (120-220Hz)
Frequency (Hz)
Z-Score

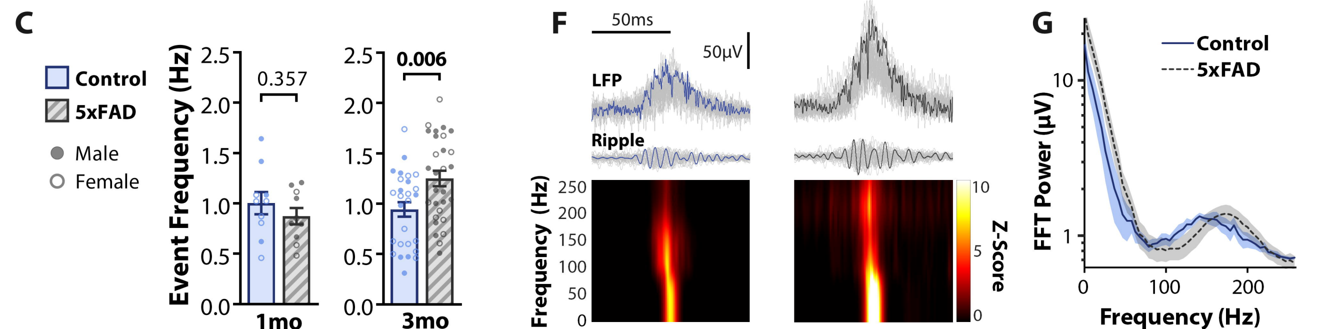
C
Control
5xFAD
Male
Female
Event Frequency (Hz)
0.357
0.006
1mo
3mo
F
50ms
50μV
LFP
Ripple
Frequency (Hz)
Z-Score
G
Control
5xFAD
FFT Power (μV)
Frequency (Hz)

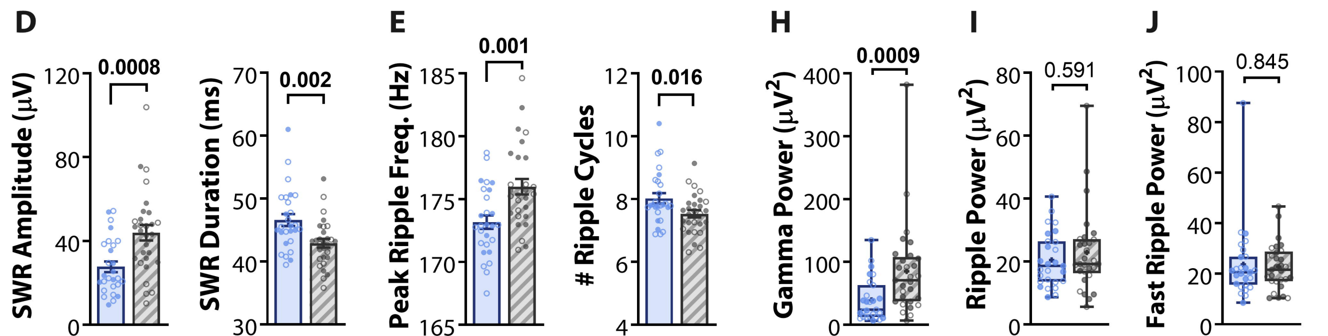
D
SWR Amplitude (μV)
0.0008
SWR Duration (ms)
0.002
E
Peak Ripple Freq. (Hz)
0.001
Ripple Cycles
0.016
H
Gamma Power (μV²)
0.0009
I
Ripple Power (μV²)
0.591
J
Fast Ripple Power (μV²)
0.845

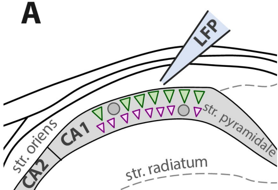
A
LFP
CA1
CA2
str. oriens
str. pyramidale
str. radiatum

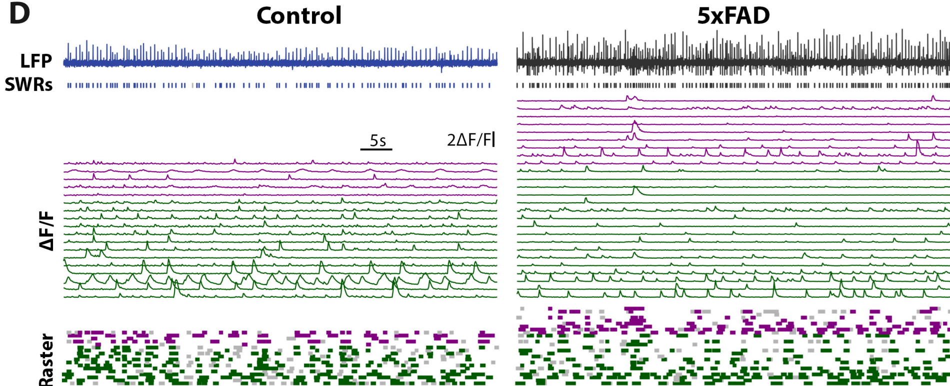
D
Control
5xFAD
LFP
SWRs
5s
2ΔF/F
ΔF/F
Raster

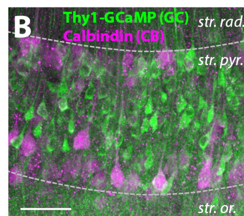
B
Thy1-GCaMP (GC)
Calbindin (CB)
str. rad.
str. pyr.
str. or.

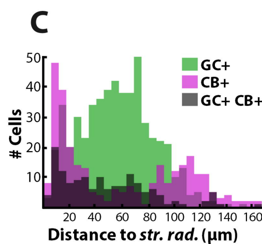
C
GC+
CB+
GC+ CB+
Cells
Distance to str. rad. (µm)

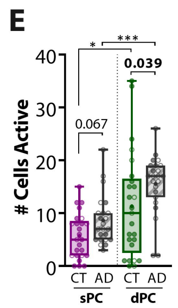
E
Cells Active
0.067
0.039
CT AD CT AD
sPC dPC

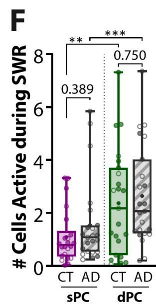
F
Cells Active during SWR
0.389
0.750
CT AD CT AD
sPC dPC

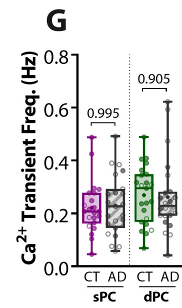
G
Ca2+ Transient Freq. (Hz)
0.995
0.905
CT AD CT AD
sPC dPC

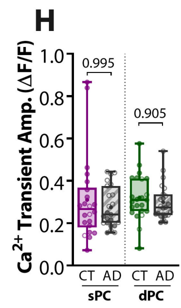
H
Ca2+ Transient Amp. (ΔF/F)
0.995
0.905
CT AD CT AD
sPC dPC

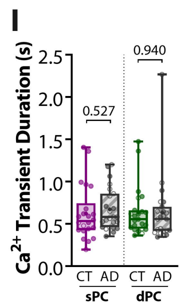
I
Ca2+ Transient Duration (s)
0.527
0.940
CT AD CT AD
sPC dPC

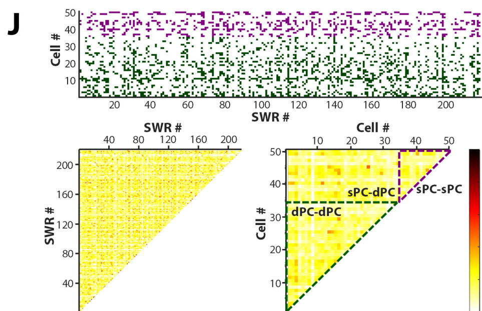
J
Cell #
SWR #
Similarity
sPC-dPC
sPC-sPC
dPC-dPC

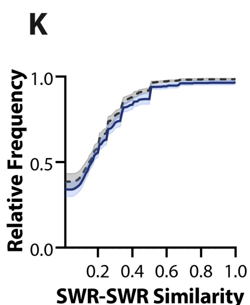
K
Relative Frequency
SWR-SWR Similarity

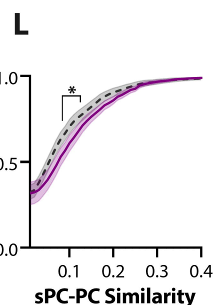
L
sPC-PC Similarity

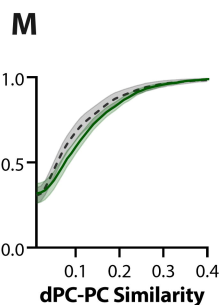
M
dPC-PC Similarity

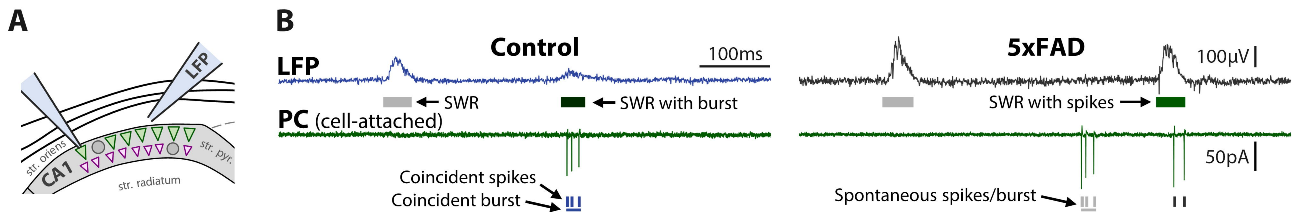

A
LFP
str. oriens
CA1
str. pyr.
str. radiatum
B
Control
LFP
100ms
SWR
SWR with burst
PC (cell-attached)
Coincident spikes
Coincident burst
5xFAD
100µV
SWR with spikes
50pA
Spontaneous spikes/burst

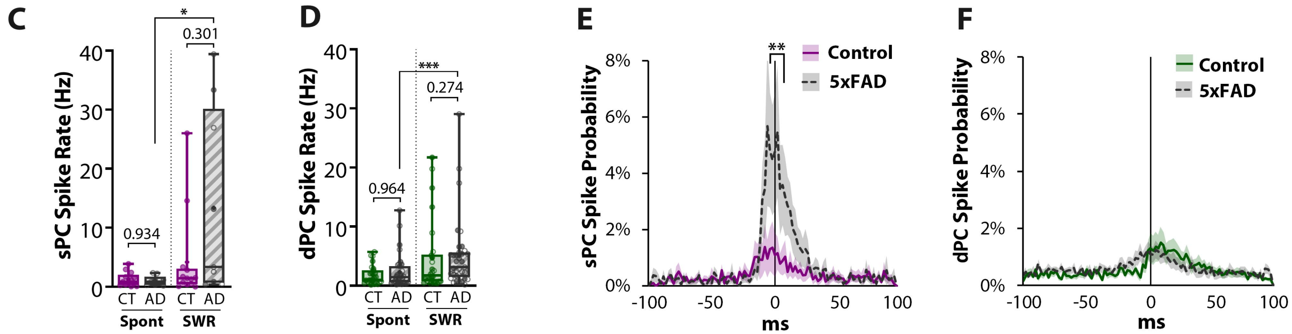

C
sPC Spike Rate (Hz)
0.934
0.301
*
CT AD CT AD
Spont SWR
D
dPC Spike Rate (Hz)
0.964
0.274
***
CT AD CT AD
Spont SWR
E
sPC Spike Probability
**
Control
5xFAD
ms
F
dPC Spike Probability
Control
5xFAD
ms

G
Burst Rate (Hz)
0.337
0.885
CT AD CT AD
sPC dPC
H
Intra-Burst Interval (ms)
0.997
0.045
CT AD CT AD
sPC dPC
I
frac. Spikes with SWR
0.424
0.142
CT AD CT AD
sPC dPC
J
frac. SWRs with Spike
0.208
0.497
CT AD CT AD
sPC dPC
K
20ms
100µV
LFP
Gamma
0°
180°
Ripple
0°
180°
PC
25pA
L
Gamma Phase-locking
90
180
0
270
0.091
0.5
1.0
N
Ripple Phase-locking
90
180
0
0.5
1.0
0.528
M
90
0
270
**
0.147
0.5
1.0
O
90
0
270
0.5
1.0
0.528

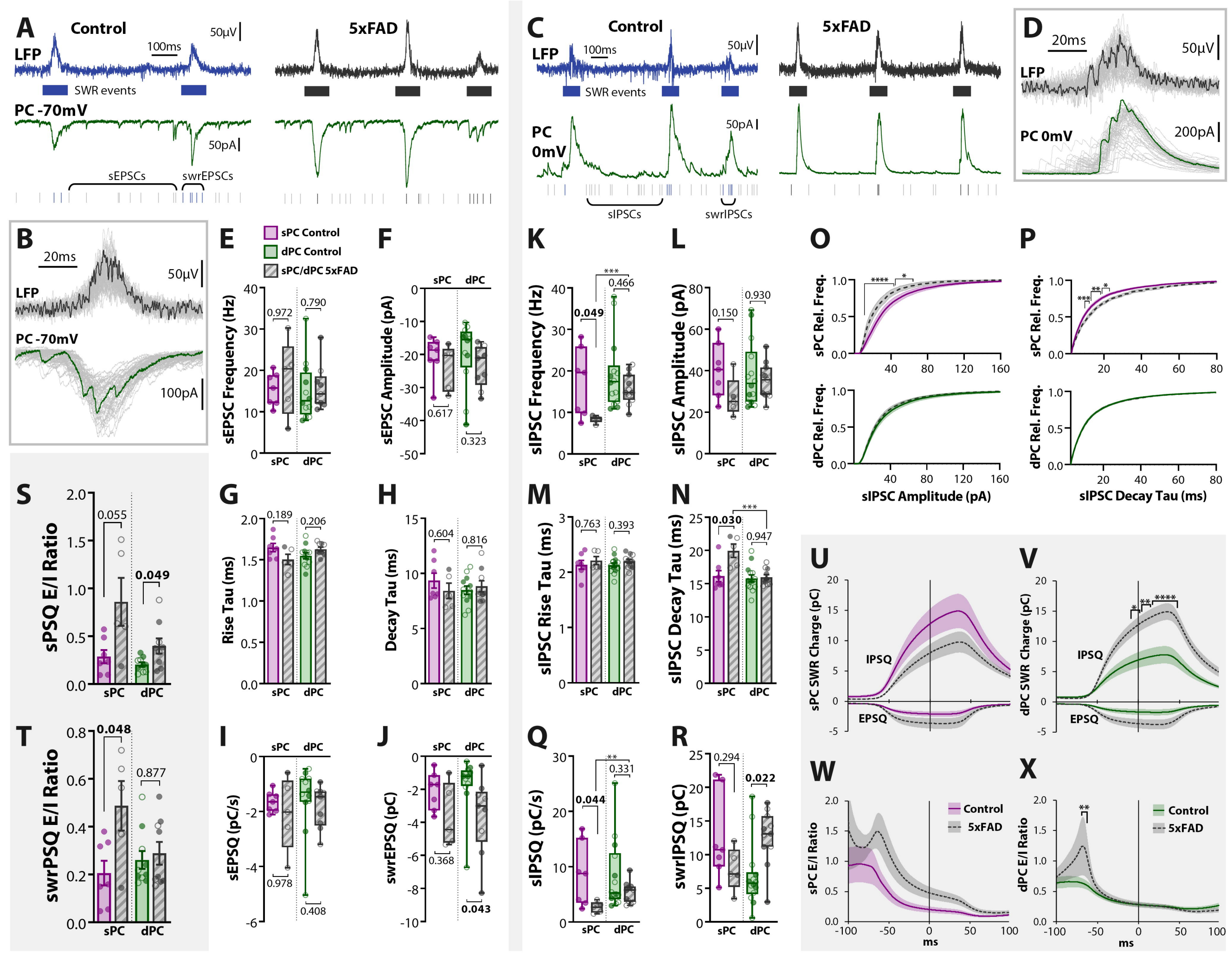

A
Control
5xFAD
LFP
50µV
100ms
SWR events
PC -70mV
50pA
sEPSCs
swrEPSCs
C
Control
5xFAD
LFP
100ms
50µV
SWR events
PC 0mV
50pA
sIPSCs
swrIPSCs
D
20ms
50µV
LFP
PC 0mV
200pA
B
20ms
50µV
LFP
PC -70mV
100pA
sPC Control
dPC Control
sPC/dPC 5xFAD
sEPSC Frequency (Hz)
sEPSC Amplitude (pA)
sIPSC Frequency (Hz)
sIPSC Amplitude (pA)
sIPSC Amplitude (pA)
sIPSC Decay Tau (ms)
sPC Rel. Freq.
dPC Rel. Freq.
sPSQ E/I Ratio
swrPSQ E/I Ratio
Rise Tau (ms)
Decay Tau (ms)
sIPSC Rise Tau (ms)
sIPSC Decay Tau (ms)
sEPSQ (pC/s)
swrEPSQ (pC)
sIPSQ (pC/s)
swrIPSQ (pC)
sPC SWR Charge (pC)
dPC SWR Charge (pC)
IPSQ
EPSQ
sPC E/I Ratio
dPC E/I Ratio
Control
5xFAD
ms
sPC
dPC

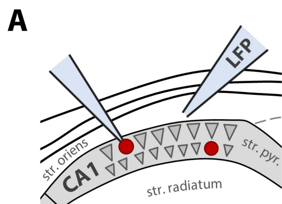
A
LFP
str. oriens
CA1
str. pyr.
str. radiatum

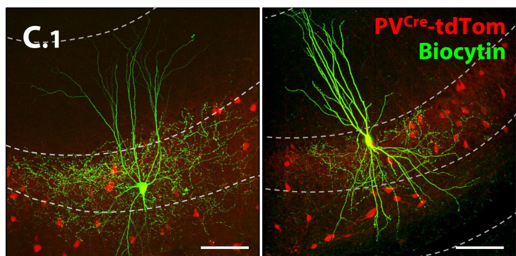
C.1
PVCre-tdTom
Biocytin
LFP
50µV
100ms
PVBC (cell-attached)
50pA

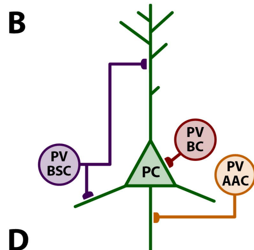
B
PV BC
PV BSC
PC
PV AAC

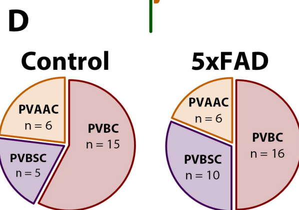
D
Control
5xFAD
PVAAC n = 6
PVBC n = 15
PVBSC n = 5
PVAAC n = 6
PVBC n = 16
PVBSC n = 10

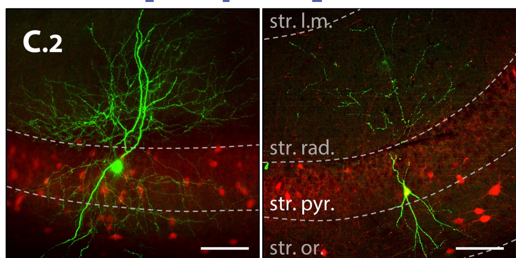
C.2
str. l.m.
str. rad.
str. pyr.
str. or.

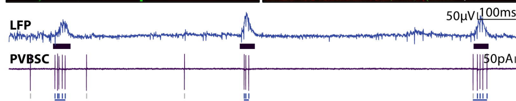
LFP
50µV
100ms
PVBSC
50pA

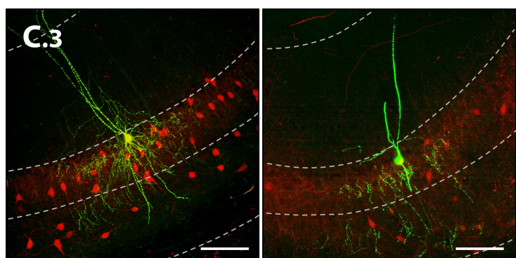
C.3
C.4
Biocytin
Ankyrin G
LFP
50µV
100ms
PVAAC
50pA

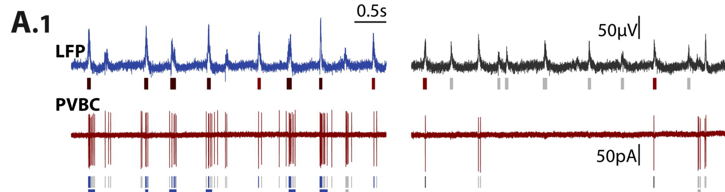
A.1
LFP
PVBC
0.5s
50µV
50pA
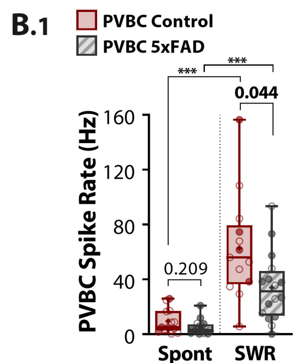
B.1
PVBC Control
PVBC 5xFAD
***
***
0.044
0.209
PVBC Spike Rate (Hz)
Spont
SWR
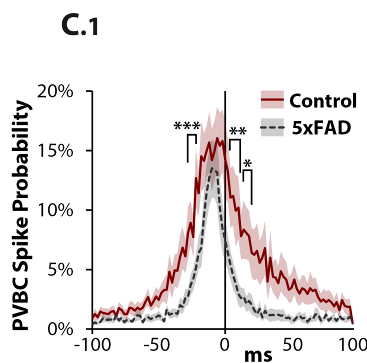
C.1
Control
5xFAD
***
**
*
PVBC Spike Probability
ms
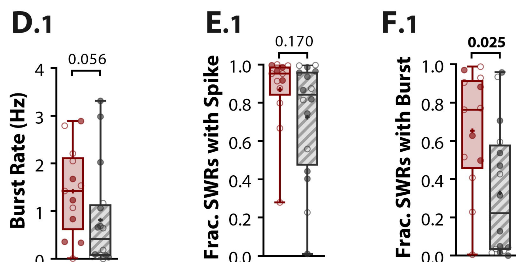
D.1
0.056
Burst Rate (Hz)
E.1
0.170
Frac. SWRs with Spike
F.1
0.025
Frac. SWRs with Burst
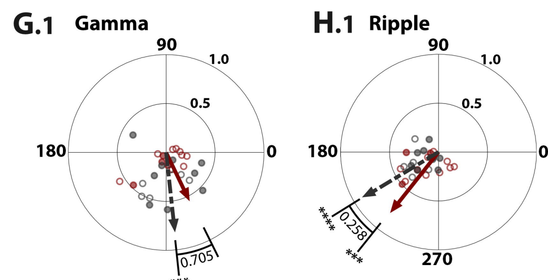
G.1 Gamma
H.1 Ripple
0.705
***
****
0.258
***
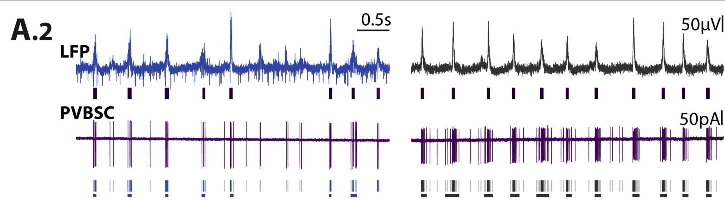
A.2
LFP
PVBSC
0.5s
50µV
50pA
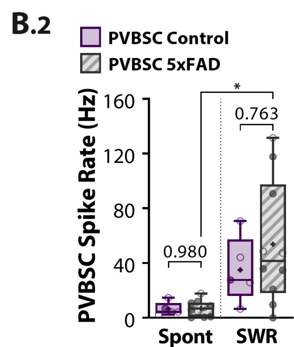
B.2
PVBSC Control
PVBSC 5xFAD
*
0.763
0.980
PVBSC Spike Rate (Hz)
Spont
SWR
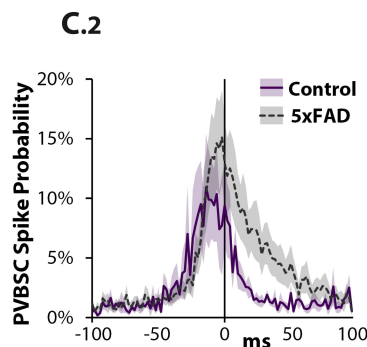
C.2
Control
5xFAD
PVBSC Spike Probability
ms
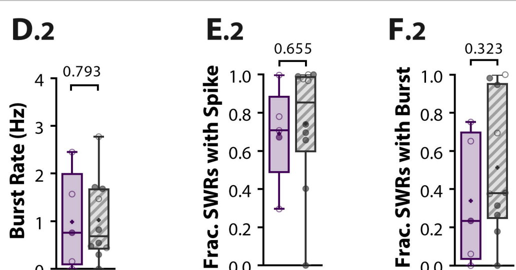
D.2
0.793
Burst Rate (Hz)
E.2
0.655
Frac. SWRs with Spike
F.2
0.323
Frac. SWRs with Burst
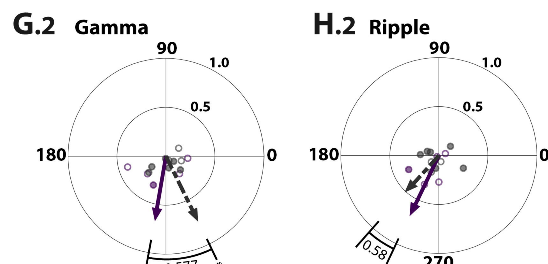
G.2 Gamma
H.2 Ripple
0.577
*
0.58
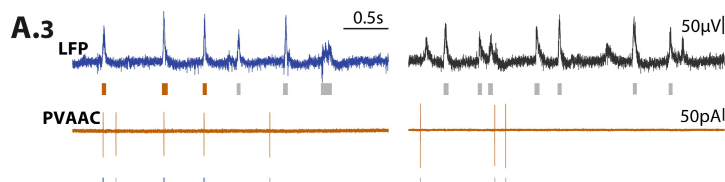
A.3
LFP
PVAAC
0.5s
50µV
50pA
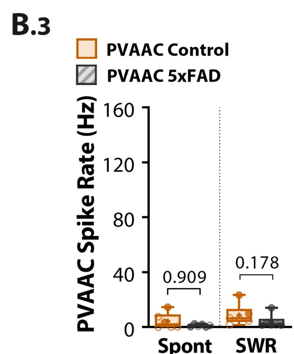
B.3
PVAAC Control
PVAAC 5xFAD
0.909
0.178
PVAAC Spike Rate (Hz)
Spont
SWR
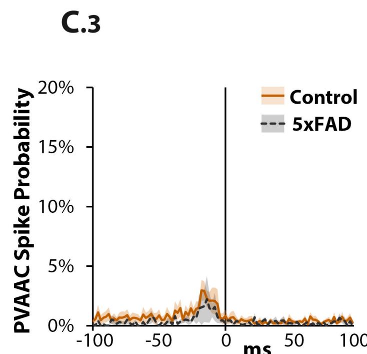
C.3
Control
5xFAD
PVAAC Spike Probability
ms
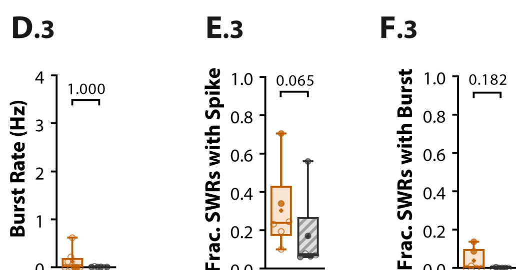
D.3
1.000
Burst Rate (Hz)
E.3
0.065
Frac. SWRs with Spike
F.3
0.182
Frac. SWRs with Burst
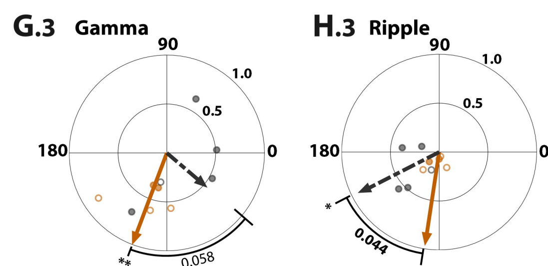
G.3 Gamma
H.3 Ripple
**
0.058
*
0.044
*

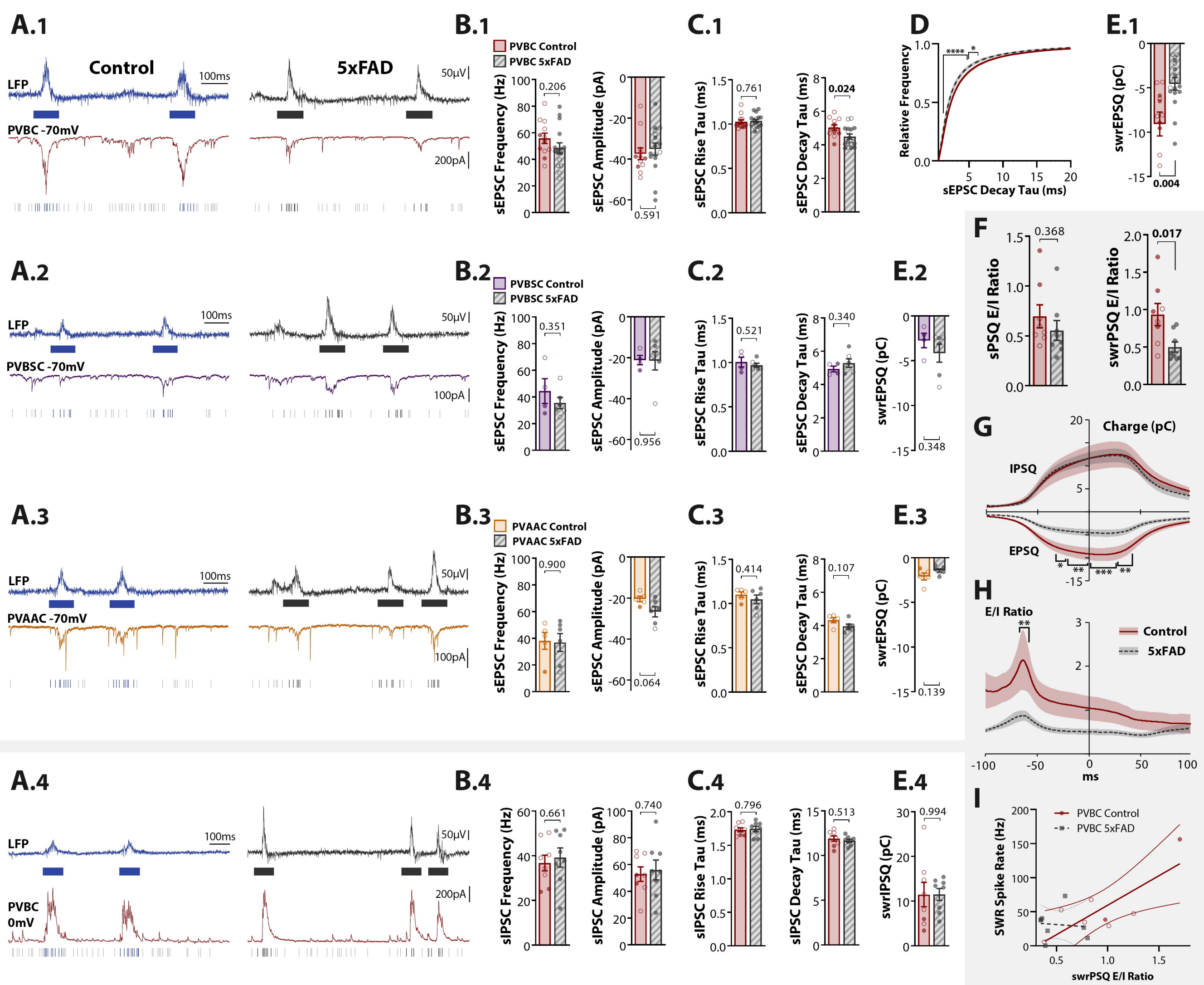

A.1
Control
5xFAD
LFP
100ms
50µV
PVBC -70mV
200pA
B.1
PVBC Control
PVBC 5xFAD
sEPSC Frequency (Hz)
0.206
sEPSC Amplitude (pA)
0.591
C.1
sEPSC Rise Tau (ms)
0.761
sEPSC Decay Tau (ms)
0.024
D
Relative Frequency
sEPSC Decay Tau (ms)
****
*
E.1
swrEPSQ (pC)
0.004
A.2
PVBSC -70mV
100pA
B.2
PVBSC Control
PVBSC 5xFAD
0.351
0.956
C.2
0.521
0.340
E.2
0.348
A.3
PVAAC -70mV
B.3
PVAAC Control
PVAAC 5xFAD
0.900
0.064
C.3
0.414
0.107
E.3
0.139
F
sPSQ E/I Ratio
0.368
swrPSQ E/I Ratio
0.017
G
Charge (pC)
IPSQ
EPSQ
H
E/I Ratio
Control
5xFAD
ms
A.4
PVBC 0mV
B.4
sIPSC Frequency (Hz)
0.661
sIPSC Amplitude (pA)
0.740
C.4
sIPSC Rise Tau (ms)
0.796
sIPSC Decay Tau (ms)
0.513
E.4
swrIPSQ (pC)
0.994
I
PVBC Control
PVBC 5xFAD
SWR Spike Rate (Hz)
swrPSQ E/I Ratio

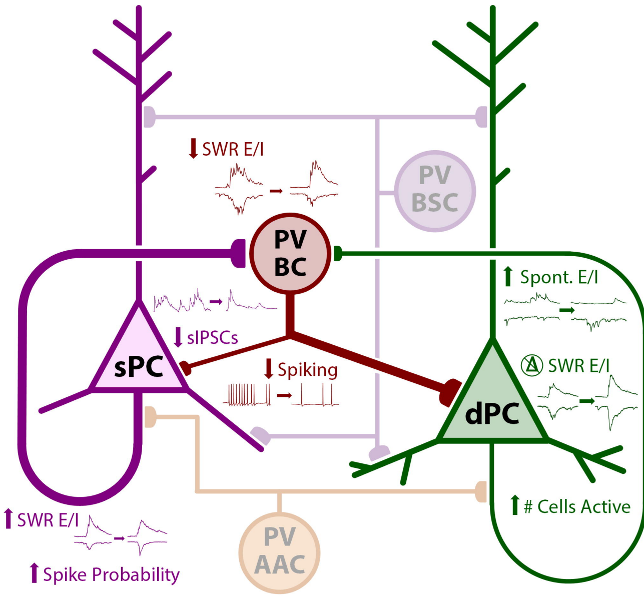

SWR E/I
PV
BSC
PV
BC
Spont. E/I
sIPSCs
sPC
Spiking
SWR E/I
dPC
Cells Active
SWR E/I
Spike Probability
PV
AAC